CRITICAL LAYERS AND PROTOPLANETARY DISK TURBULENCE.

Orkan M. Umurhan[1], Karim Shariff and Jeffrey N. Cuzzi
NASA Ames Research Center, Moffett Field, CA 94053, U.S.A
(Dated:)
Draft version January 5, 2016

ABSTRACT

A linear analysis of the zombie vortex instability is performed in a stratified shearing sheet setting for three model barotropic shear flows: the vorticity step, the shear layer and the asymmetric jet. The examination assumes that both disk-normal gravity and stratification is constant. The aim is to better understand the instability of so-called Z-modes and the subsequent nonlinear self-reproduction process discussed in the literature. The linear analysis is done by utilizing a Green's function formulation to resolve the critical layers of the associated normal-mode problem. We report several results: The instability is the result of a resonant interaction between a Rossby wave and a gravity wave. The associated critical layer is the location where the Doppler shifted frequency of a distant Rossby wave equals the local Brunt-Väisälä frequency. In the shear flow model, parameter value sweeps are done to determine when unstable Z-modes exist both separately of and in conjunction with the Rossby wave instability. The minimum required Rossby number for instability, $\mathtt{Ro} = 0.2$, is confirmed for parameter values previously examined in the literature. It is also found that the shear layer supports the instability in the limit where stratification vanishes. The zombie vortex instability as well as the Rossby wave instability are examined for the first time in a jet model, finding that the instability can occur for $\mathtt{Ro} = 0.05$. For all model flows considered, nonlinear vorticity forcing due to unstable Z-modes is shown to result in the creation of a jet flow at the critical layer. The jet-flow emerges as the result of the competition between the vertical lifting of perturbation radial vorticity and the radial transport of vertical perturbation vorticity wherein the former mechanism usually dominates the latter. We find that the picture of this instability leading to a form of nonlinearly driven self-replicating/self-reproducing pattern of creation and destruction is warranted: parent jets spawn and grow child jets at associated critical layers and once the child jet grows strong enough it subsequently creates a next generation of jets associated with its critical layer while simultaneously destroying itself due to the Rossby wave instability. We conclude with some speculation.

Keywords: Hydrodynamics, Astrophysical Disks – theory, instabilities

1. INTRODUCTION

The last few years have enjoyed a revival in the study of non-magnetic routes to turbulence in protoplanetary disks. Mostly with the aid of high resolution numerical investigations, several new instability mechanisms and processes have been identified and shown to lead to some kind of sustained turbulent activity, including (but not limited to), the baroclinic instability (Klahr & Bodenheimer, 2003, Petersen et al. 2007a,2007b, Lesur & Papaloizou, 2010, Lyra & Klahr, 2011, Klahr & Hubbard, 2014, Lyra 2014) the Vertical Shear instability (Goldreich & Schubert, 1967, Fricke, 1968, Brandenberg and Urpin 1998, Urpin 2003, Nelson et al. 2013, Stoll & Kley 2014, VSI hereafter), and recently the self-replicating "zombie vortex" instability (Marcus et al. 2013, Marcus et al. 2015). This study is aimed at developing deeper intuition of the linear instability associated with the self-reproducing zombie mode instability (ZMI hereafter) examined in Marcus et al. (2013, M13 hereafter).

M13 uncover the ZMI via numerical simulations in a stably stratified rotating Cartesian box model known as the shearing box (Goldreich & Lynden-Bell, 1965). The model is composed of a vertical component of uniform gravity and a basic, vertically uniform, Keplerian (azimuthal) flow field varying linearly with respect to the (nominal) radial box coordinate. M13 consider the physical response of an azimuthally-aligned and relatively thin

"tube" of surplus vertical vorticity initiated in the center of the box. The tubular vortex responds to perturbations by radiating internal gravity waves which become resonant with distant buoyant critical layers. The resonant interaction at the critical layer is unstable and results in the generation of jet flows similarly oriented with the original tubular field. These "child" jets are found in planes parallel to the mid-plane containing the original "parent" tubular surplus field.

M13 show that the original parent vorticity field used to showcase this process remains stable and constituted during the growth and maturation of the children. Typically, the vorticity of the child jet grows in magnitude until it triggers a secondary roll-up type of instability and then gets destroyed. Before these first generation of jets are destroyed, however, they have enough time to spawn a second generation of jets through the same resonant critical layer interaction that brought the first generation into existence. The numerical experiments in M13 illustrate a self-reproducing process enveloping the domain, essentially "crystallizing" it by leaving behind a lattice pattern of dynamically active regions of concentrated vertical vorticity undergoing cycles of creation and destruction. The final result resembles a sustained turbulent state.

If this self-replicating process holds up to independent scrutiny, its consequences are profound as far as planet formation is concerned because such a resulting flow state has important implications with regards to dust accumulation in protoplanetary disk, magnetic-Dead-Zones

[1] Also at SETI Institute, 189 Bernardo Way, Mountain View, CA 94043, U.S.A. Email: orkan.m.umurhan@nasa.gov

of protoplanetary disks (Turner, et al., 2014). For example, a scenario often quoted is one in which steady anticylonic vortices can attract particles over time. But if this instability is active, while creating vortices it also destroys them and thereby disrupting the envisioned process of steady particle concentration. The consequence of this would be especially felt during the early stages of cold disk evolution. Equally important is that triggering this dynamical process requires a minimum source of perturbation vorticity (see also Marcus et al. 2015). Identification of this Z-mode self-replicating process in numerical experiments necessitates high resolution studies because the dynamical activity is concentrated in a narrow region centered on the critical layers wherein the region's size depends linearly on the growth rate. A similar demand on resolution is needed for the VSI, but for entirely different reasons (Nelson et al. 2013, Stoll & Kley 2014, Barker & Latter, 2015, Umurhan et al., 2015, Richard et al., 2015).

In this study we are interested in shedding some light on the mechanism of the linear instability associated with this phenomenon and, furthermore, developing some insight as to how the the critical layer instability leads to the creation of jets. The linear stability analysis of this relatively simplified shearing box setting is a notoriously difficult problem even in the case where there is only a purely Keplerian flow with no other additional vorticity surplus (e.g., Dubrulle et al. 2005). A normal mode reduction of this stripped-down linearized system produces a second order differential equation with irregular singular points and makes generating solutions, both analytically and numerically, extremely delicate and subtle. The challenges are more compounded if one attempts to linearly study the same system with the addition of the surplus vertical vorticity field considered by M13 which varies both radially and vertically. In this setting, the linear stability problem becomes inseparable in both the radial and vertical coordinates, thereby amplifying the challenges faced by the analyst.[2]

Instead, we consider the linear normal mode response in the stably stratified shearing box containing *a vertically uniform* surplus vertical vorticity field – either as a vorticity step located at the origin, or a vertically uniform shear layer, or a vertically uniform deviation jet flow (see Figure 1). By being vertically uniform, these flows are often referred to as "barotropic". These test models are chosen because of analytical and numerical tractability. While these model flow profiles are different than what was considered in M13, we find that the linear dynamical properties of these flow profiles are qualitatively similar to the processes involved in the self-reproducing mechanism reported in M13. We find:

1. The ZMI is characterized primarily as the near resonance between the Doppler shifted frequency of the Rossby wave associated with the distant surplus vorticity field and the Brunt-Väisälä frequency at the buoyant critical layer. Without the Rossby wave the buoyant critical layer is not excited.

2. The nonlinear outcome of the linear instability is

to drive into existence a jet-like vertical vorticity field at the critical layer(s).

3. The primary mechanism that spawns the jet flow is the vertical tilting of perturbation radial vorticity although the radial transport of perturbation vertical vorticity can also be important in magnitude depending upon the type of shear flow under consideration.

4. Model jet flows support both the ZMI and the familiar Rossby wave instability (Lovelace et al. 1999, Li et al. 2000, Li et al. 2001, Meheut et al. 2010, Umurhan 2010, Meheut et al. 2012, RWI hereafter), the latter of which induces nonlinear roll-up of the anticyclonic part of the jet.

5. When the amplitude of the jet's vorticity exceeds a minimum value, the jet gets destroyed by the RWI. In the Keplerian flow frame, the anti-cyclonic side of the jet experiences destructive roll-up into coherent vortices.

6. Depending upon the base flow field considered, the analysis indicates that the self-replicating ZMI can be active for surplus vorticity fields whose Rossby numbers are as small as 0.05 – a figure which is smaller than previously anticipated by about a factor of four.

This study is organized as follows: Section 2 presents the shearing box equations assumed for this analysis, including the scalings leading to them and other assumptions and simplifications. The exact nonlinear form of the vertical vorticity evolution equation is also shown. In Section 3 the linearized equations of motion are derived, assuming a (generalized) vertically uniform surplus vertical vorticity field. After stating our assumptions, it is shown how the equations of motion can be written either as a set of coupled integral equations or as a second order differential equation in the radial coordinate of the shearing box. The system is further decomposed into a potential vorticity formulation which identifies the main wave mode involved in the ZMI later explored. Section 4 presents the model surplus vorticity fields to be tested in our analysis: the vorticity step and the asymmetric jet. Section 5 details the relevant length and time scales in the problem and identifies the independent parameters of the problem depending upon which profile is considered. Section 6 discusses the general solution method implemented. Because of the aforementioned difficulties inherent to solutions of differential operators with explicitly appearing, non-removable, irregular singular points, we opt for solving the coupled integro-differential equations developed in Section 3.

Section 7 concentrates on the normal mode results for the three model shear flows considered. We detail the properties of the Zombie mode instability (herein termed Z-modes) in the simple vortex step profile. We also show how the asymmetric jet profile also supports both the Z-mode instability and the RWI (the latter detailed in Appendix B). For the latter, we analytically develop growth rates and conditions for marginality. Section 8 examines the nonlinear forcing implied by an unstable Z-mode. We explicitly demonstrate how it drives into existence

---

[2] This is also a feature of the VSI; see the discussion in Barker & Latter (2015) and Umurhan et al. (2015).

a jet flow at the location of the critical layer. Section 9 summarizes our main results and interprets the self-replicating dynamical process of jet creation/destruction in terms of the physical results garnered by the examination peformed in this study.

2. EQUATIONS

Following M13, we consider dynamics in the so-called shearing box which represents dynamics in the frame of a Cartesian "box"-section of an accretion disk which rotates around the central star at a distance of R_0 with a rotation rate Ω_0 and corresponding rotation vector given by $\hat{\mathbf{z}}\Omega_0$, (see Goldreich & Lynden-Bell, 1965) which is aligned with the disk vertical direction. We take the equivalent radial direction to be along $\hat{\mathbf{x}}$ and the disk's azimuthal direction vector as $\hat{\mathbf{y}}$. Length scales in the box are in units of the local vertical scale height H_0. The box equations are considered valid because the ratio H_0/R_0 is generally small for cold accretion disks. We make the additional assumption of a Boussinesq fluid and, thereby, suppressing acoustic modes. The equations of motion are therefore

$$(\partial_t + u\partial_x + v\partial_y + w\partial_z)u - 2\Omega_0 v = -\partial_x\Pi + 3\Omega_0^2 x, \quad (1)$$

$$(\partial_t + u\partial_x + v\partial_y + w\partial_z)v + 2\Omega_0 u = -\partial_y\Pi, \quad (2)$$

$$(\partial_t + u\partial_x + v\partial_y + w\partial_z)w = -\partial_z\Pi + g\Theta, \quad (3)$$

$$(\partial_t + u\partial_x + v\partial_y + w\partial_z)\Theta + \beta w\Theta = 0, \quad (4)$$

$$\partial_x u + \partial_y v + \partial_z w = 0. \quad (5)$$

The quantities u, v, w denote the components of velocity in the radial, azimuthal and vertical directions respectively. In the shearing box, the u, v and w velocity components are scaled by the local sound speed and this is possible only because the box equations are for dynamics in a frame moving with the exceedingly faster Keplerian velocity. To facilitate comparison with the results of M13, we make the similar assumption that is made in that study wherein the vertical component of the disk gravitational field g is taken to be a constant.

The quantity Θ can be interchangeably interpreted as either an entropy or a buoyancy; for this analysis we consider it as the latter, in which case Θ is a non-dimensional quantity by definition. Equation (3) says the entropy/buoyancy field is passively advected by the total flow with no sources or sinks meaning to say that the perturbations are adiabatic. Implicitly, we are saying that the actual cooling times of the protoplanetary disk gas is much longer than the growth rates calculated later on. [3] Because we are in the Boussinesq approximation, the pressure field p is rewritten in terms of the quantity $\Pi \equiv p/\rho_0$, as the density ρ_0 is taken to be a constant in the mean state. The quantity β, which is in units of inverse length, represents the vertical gradient of the disk buoyancy (itself a dimensionless quantity) and as with g above, we assume it is constant. As taken here, $\beta > 0$ means that it is buoyantly stable and the model is stably stratified against buoyant instabilities.

In deriving the box equations, there is always a component representing the radial gradient of the gravitational

---

[3] This is in contrast with the conditions giving rise to the VSI which requires cooling times to be very short compared to both the local rotation time of the disk and the associated growth rates. See recent discussion in Lin & Youdin (2015).

potential of the central star, and this appears in the form of the expression $3\Omega_0^2 x$ found on the right hand side of the x-momentum equation. In the absence of time dependent dynamics, the balance of this term with the corresponding Coriolis term $-2\Omega_0 v$ admits the basic Keplerian flow state v_k, i.e.

$$-2\Omega_0 v_k = 3\Omega_0^2 x, \qquad \longrightarrow \quad v_k = -\frac{3}{2}\Omega_0 x.$$

However, in this study, we shall consider arbitrary plane parallel shear flows $v_0(x)$ containing both v_k plus some deviation/surplus shear flow V_0, the latter of which is similarly scaled by the local sound speed. Such a deviation flow is a steady solution of this system provided the pressure field shows some radial variation in its steady state as well:

$$v_0(x) = v_k + V_0, \quad (6)$$

where $V_0 = (\partial_x\Pi_0)/(2\Omega_0)$ is the departure from the basic Keplerian flow v_k. We detail in Section 4 the two types of V_0 we analyze herein. We often refer to these flow fields as *barotropic flow profiles* since we assume there is no vertical variation of V_0.

Although this is primarily a linear stability analysis, the nonlinear vertical vorticity equation is useful in helping us to interpret the consequences of the results we report here in this work. We define the vertical component of the fluid vorticity as

$$\zeta \equiv \partial_x v - \partial_y u.$$

In order to obtain an evolution equation for this quantity we operate on equation (2) by ∂_x and subtract from it the result of operating on equation (1) by ∂_y. Rearranging the result and making use of (5) we find

$$\left(\partial_t + u\partial_x + v\partial_y + w\partial_z\right)\zeta =$$

$$(2\Omega_0 + \zeta)\partial_z w - \left[(\partial_x w)\cdot(\partial_z v) - (\partial_y w)\cdot(\partial_z u)\right]. \quad (7)$$

What this equation says is that the vertical vorticity is advected (in a Lagrangian sense) by the flow field and, had the right hand side of the above equation been zero, the local value of ζ would be preserved along the way. However, at any given position, ζ can change because of the two effects appearing on the right hand side of equation (7). The first of these, arising from the expression $(2\Omega_0 + \zeta)\partial_z w$, is the familiar effect of vertical stretching wherein the total vorticity contained in a moving fluid element can spin up or down depending upon whether or not there is concurrent vertical stretching in the flow field itself. This is the usual effect known from the study of Taylor columns. The remaining terms can be rewritten to represent the well-known vortex tilting effects,

$$= -\left[(\partial_x w)\cdot(\partial_z v) - (\partial_y w)\cdot(\partial_z u)\right],$$

$$= \left(\partial_y w - \partial_z v\right)\partial_x w + \left(\partial_z u - \partial_x w\right)\partial_y w,$$

$$= \zeta_x\partial_x w + \zeta_y\partial_y w, \quad (8)$$

where the x and y directed vorticities are defined by $\zeta_x \equiv \partial_y w - \partial_z v$ and $\zeta_y \equiv \partial_z u - \partial_x w$ respectively. For example, the expression $\zeta_x\partial_x w$ describes the rate in which the x-directed component of the vorticity is turned into

vertical vorticity due to the shear along the x-direction of the vertical velocity field w. A similar interpretation holds for the term $\zeta_y \partial_y w$. [4] We find below that when the so-called zombie modes appear, they lead to nonlinear generation of vertical vorticity through the combined action of the two vortex tilting terms shown in expression (8). We find that between the two, the vortex tilting generation of vertical vorticity is usually by the $\zeta_x \partial_x w$ term.

3. LINEARIZATION

We linearize around a plane-parallel shear state by introducing the form

$$\left(u, v, w, \Pi, \Theta\right)^{\mathrm{T}} \mapsto \left(0, v_0(x), 0, \Pi_0(x), 0\right)^{\mathrm{T}} +$$

$$\left(u'(x,t), v'(x,t), w'(x,t), \Pi'(x,t), \Theta'(x,t)\right)^{\mathrm{T}} e^{i(\alpha y + mz)} + \text{c.c.},$$

where the T superscript means transpose, $v_0(x) = -3x\Omega_0/2 + V_0(x)$, in which $V_0(x)$ is the aforementioned arbitrary barotropic shear profile of our choosing. The above ansatz inserted into the equations of motion yields the following partial differential equations for the perturbation quantities,

$$\left(\partial_t + i\alpha v_0\right)u' - 2\Omega_0 v' = -\partial_x \Pi', \quad (9)$$

$$\left(\partial_t + i\alpha v_0\right)v' + (2\Omega_0 + v_{0x})v' = -i\alpha \Pi', \quad (10)$$

$$\left(\partial_t + i\alpha v_0\right)w' = -im\Pi' + g\Theta', \quad (11)$$

$$\left(\partial_t + i\alpha v_0\right)\Theta' = -\beta w', \quad (12)$$

$$\partial_x u' + i\alpha v' + imw' = 0. \quad (13)$$

Our subsequent analysis exploits the incompressible nature of the disturbances. This is done by reducing the linearized equations of motion into vorticity/dilatational form, i.e., by defining (respectively) the vertical vorticity perturbation and horizontal velocity divergence according to

$$\zeta' \equiv \partial_x v' - i\alpha u', \qquad D' \equiv \partial_x u' + i\alpha v'. \quad (14)$$

The horizontal velocity fields may be written in velocity-potential/streamfunction form, i.e.,

$$u' = -i\alpha \psi' + \partial_x \phi', \qquad v' = \partial_x \psi' + i\alpha \phi' \quad (15)$$

where ψ' and ϕ are the streamfunction and velocity-potentials, respectively. The above formulation automatically satisfies the incompressibility equation (14) provided

$$\zeta' = (\partial_x^2 - \alpha^2)\psi', \qquad D' \equiv -imw' = (\partial_x^2 - \alpha^2)\phi', \quad (16)$$

noting here that the vertical velocity is equated with the horizontal divergence based on the above form. The equations of motion may now be formally reduced by one

---

[4] This is a well-known feature in incompressible rotating flows where, in general vector form, the vorticity equation reads

$$\frac{d\omega}{dt} = (\omega \cdot \nabla)\mathbf{u},$$

where $\omega = 2\Omega_0 \hat{\mathbf{z}} + \zeta$ with $\zeta \equiv \nabla \times \mathbf{u}$ with $\mathbf{u}$ the vector velocity field.

---

order in time derivatives to get the following

$$\left(\partial_t + i\alpha v_0\right)\zeta' = -(2\Omega_0 + v_{0x})D' - v_{0xx}u', \quad (17)$$

$$\left(\partial_t + i\alpha v_0\right)D' = -m^2\Pi' - \theta', \quad (18)$$

$$\left(\partial_t + i\alpha v_0\right)\theta' = \beta g D', \quad (19)$$

where we have defined the quantity $\theta' \equiv im\Theta'$. Note that throughout this study we assume stable stratification which means that the Brunt-Väisälä frequency N_B is real, i.e. $N_B^2 \equiv g\beta > 0$. As far as nomenclature is concerned, we mostly dispense with using the symbol N_B for the Brunt-Väisälä frequency and, instead, retain for its designation the expression $g\beta$.

The above third order system (in time) is supplemented by the diagnostic condition relating the perturbation pressure to the other quantities appearing, and is given as the solution of

$$\left(\partial_x^2 - \alpha^2 - m^2\right)\Pi' = 2\Omega_0 \zeta' + \theta' - 2i\alpha v_{0x}u'. \quad (20)$$

We observe that the vertical vorticity field is driven by vertical stretching (D') and radial advection of the mean vorticity gradient ($v_{0xx}u'$).

In the form as developed here, the streamfunction and velocity potential solutions are written in terms of Green's functions, i.e.

$$\psi' = \int G_\psi(x, x')\zeta'(x')dx',$$

$$\phi' = \int G_\phi(x, x')D'(x')dx', \quad (21)$$

where $G(x, x')$ is the appropriate Green's function associated with the two-dimensional Laplace operator $\partial_x^2 - \alpha^2$, *subject to appropriate boundary conditions (see more below)*,

$$\left(\partial_x^2 - \alpha^2\right)G_{\phi,\psi} = \delta(x - x'), \quad (22)$$

where $\delta(x)$ is the Dirac delta function. Similarly, the corresponding solution of the pressure fluctuations is given by

$$\Pi' = \int G_\Pi(x, x')\left\{2\Omega_0 \zeta'(x') + \theta'(x') - 2i\alpha v_{0x}(x')u'(x')\right\}dx'. \quad (23)$$

The Green's function G_Π is the solution of

$$\left(\partial_x^2 - k^2\right)G_\Pi = \delta(x - x'), \qquad k^2 \equiv \alpha^2 + m^2. \quad (24)$$

The system of equations (17–20) together with their associated diagnostic relationships (15) and (16) is an integro-differential system which must be solved subject to boundary conditions in the radial direction. The Green's function strategy adopted here has been used in other disk studies (e.g., Dubrulle & Knobloch, 1992). For this study we report upon solutions in which all quantities exponentially decay to zero as $x \to \pm\infty$. We note that for the unstable localized modes which are the subject of this study, we have checked and verified that the results reported here are insensitive to whether or not the perturbations are periodic (on scale $2L$) or if there are no-normal flow boundary conditions imposed at $x = \pm L$.

The above statement becomes robust so long as the horizontal domain is large enough with, typically speaking, $L \geq \pi$. The location of truncation scale L does not interfere with the existence and/or expression of an unstable mode.

3.1. An alternative form in terms of a perturbation potential vorticity

It is worth noting that the processed linearized equations (17–19) may be recast instead in terms of a perturbation vertical *potential vorticity*, Ξ', defined by

$$\Xi' \equiv \zeta' + \left(\frac{2\Omega_0 + v_{0x}}{\beta g}\right)\theta', \tag{25}$$

The perturbation equations may now be rewritten in the following alternative formulation:

$$\left(\partial_t + i\alpha v_0\right)\Xi' = -v_{0xx}u', \tag{26}$$

$$\left(\partial_t + i\alpha v_0\right)\zeta' = -(2\Omega_0 + v_{0x})D' - v_{0xx}u', \tag{27}$$

$$\left(\partial_t + i\alpha v_0\right)D' = -m^2\Pi' + \frac{g\beta}{2\Omega_0 + v_{0x}}\left(\zeta' - \Xi'\right), \tag{28}$$

with

$$\left(\partial_x^2 - k^2\right)\Pi' = \left[\frac{2\Omega_0(2\Omega_0 + v_{0x}) - g\beta}{2\Omega_0 + v_{0x}}\right]\zeta'$$
$$- 2i\alpha v_{0x}u' + \frac{g\beta}{2\Omega_0 + v_{0x}}\Xi'. \tag{29}$$

We note immediately that in the event that v_{0x} is constant (e.g. pure Keplerian flow with $V_0 = 0$), the system materially conserves the perturbation potential vorticity with the basic constant shear state. In slightly more general terms, if $V_0(x) = \overline{\Omega_x}x$, where $\overline{\Omega_x} = $ constant (units of inverse time), then

$$\left(\partial_t + i\alpha qx\right)\Xi' = 0, \qquad q = -\frac{3}{2}\Omega_0 + \overline{\Omega}_x, \tag{30}$$

which means that a potential vorticity perturbation is advected by the composite background shear flow field $= qx$. In this way the system becomes relatively transparent. In the event we consider a flow field such that $v_{0xx} = 0$, together with $\Xi' = 0$ initially, then the linear response is of pure inertial gravity waves.

3.2. As a single second order differential equation and critical layers

Previous treatments (e.g., Dubrulle et al. 2005) of this system as a normal mode problem have instead turned equations $(9 - 14)$ into a single second order differential equation. Indeed, combining these equations into a single one for the normal-mode pressure perturbation results in

$$\left(\partial_x^2 - k^2\right)\hat{\Pi} = 2\Omega_0\hat{\zeta} + \hat{\theta} - 2i\alpha v_{0x}\hat{u}, \tag{31}$$

in which the following normal mode ansatz has been assumed

$$\Pi' = \hat{\Pi}(x)e^{-i\omega t}, \tag{32}$$

and similarly for the other quantities appearing. Here, ω is the unknown complex normal mode frequency. Insertion of this form into the fundamental perturbation equations (9–14) followed by some manipulation shows that

the following relationships hold between various quantities:

$$\hat{\theta} = \frac{g\beta m^2}{\sigma^2 - g\beta}\hat{\Pi}, \qquad \hat{D} = \frac{i\sigma}{g\beta}\hat{\theta} = \frac{i\sigma m^2}{\sigma^2 - g\beta}\hat{\Pi},$$

$$\hat{u} = \frac{2\Omega_0\alpha\hat{\Pi} + \sigma\partial_x\hat{\Pi}}{\omega_\varepsilon^2 - \sigma^2}, \tag{33}$$

as well as

$$2\Omega_0\hat{\zeta} = -\frac{\omega_\varepsilon^2}{g\beta}\hat{\theta} - 2\Omega_0 v_{0xx}i\sigma\hat{u}, \tag{34}$$

where we have defined $\sigma(x) \equiv \alpha v_0(x) - \omega$ and $\omega_\varepsilon^2(x) \equiv 2\Omega_0(2\Omega_0 + v_{0x}(x))$ - the latter of these is the local disk epicyclic frequency. Rewriting equation (20) in terms of the normal mode ansatz means that

$$\left(\partial_x^2 - \alpha^2 - m^2\right)\hat{\Pi} = 2\Omega_0\hat{\zeta} + \hat{\theta} - 2i\alpha v_{0x}\hat{u}, \tag{35}$$

and making use of the above relationships and some additional reduction shows that

$$\left(\partial_x^2 - k^2\right)\hat{\Pi} = \frac{\omega_\varepsilon^2 - g\beta}{g\beta - \sigma^2}m^2\hat{\Pi}$$
$$+ \frac{1}{\sigma^2 - \omega_\varepsilon^2}\left(2\alpha v_{0x} - \frac{2\Omega_0 v_{0xx}}{\sigma}\right)\left(2\Omega_0\alpha\hat{\Pi} + \sigma\partial_x\hat{\Pi}\right) \tag{36}$$

This system is subject to the same boundary conditions as outlined above. [5]

Inspection of the ODE (36) shows that there exists the possibility of several critical layers in the system. Locations where the denominators vanish are candidate irregular singular points. Of interest to us are the points associated with expressions multiplying the pressure $\hat{\Pi}$ (and, not any of its derivative expressions). These points become irregular if the denominators or the associated expressions can pass through zero linearly with respect to variations in x. Several candidate points are identified: The first of these is the classical one associated plane parallel shear flows and occurs at points x_{pp} in which $\mathrm{Re}(\sigma) = 0$, i.e.

$$\alpha v_0(x_{pp}) - \mathrm{Re}(\omega) = 0.$$

In classical plane parallel shear flow problems, such critical layers activate only if both $v_{0xx} \neq 0$ and if viscosity is included (Drazin & Reid, 1981). The normal modes associated with these critical layers are called Tollmien-Schlichting waves (TS waves) and they are unstable for wide values of Reynolds numbers. TS-waves cease to be normal modes in the exactly inviscid problem. In monotonic shear flows (flows in which the shear velocity strictly increases or decreases) there tends to be only one such critical point x_{pp}.

With the inclusion of buoyancy under stable stratification, in which $g\beta > 0$, two more critical layers emerge at points $x_{bg}^\pm$ which we henceforth refer to as *buoyant critical layers* to distinguish them from the others. These

---

[5] Had we considered no-normal flow boundary conditions at $x = \pm L$, then the imposition of an impenetrable flow boundary condition at these two locations would be the same as imposing

$$2\Omega_0\alpha\hat{\Pi} + \sigma\partial_x\hat{\Pi} = 0,$$

at $x = \pm L$ provided $\sigma^2 - \omega_\varepsilon^2 \neq 0$ at the boundaries.

locations are associated with the first term on the right hand side of equation (36), where $\mathrm{Re}(\sigma) \pm \sqrt{g\beta} = 0$, i.e.

$$\alpha v_0\left(x_{b_g}^{\pm}\right) \pm \sqrt{g\beta} - \mathrm{Re}(\omega) = 0. \qquad (37)$$

The instability identified in Section 7 pertains to the action of these buoyant critical layers. An inspection of equation (36) shows that these critical layers are intrinsically a three-dimensional phenomenon as the expression $m^2\hat{\Pi}/(g\beta - \sigma^2)$ requires vertical perturbations ($m \neq 0$), azimuthal perturbations ($\alpha \neq 0$) and a radial variation in the shear flow $v_0(x)$.

Finally, equation (36) also admits the possibility of two more critical layers associated with those points where the denominator of the second term on the right hand side of equation (36) is equal to zero, that is, $\mathrm{Re}(\sigma) \pm \omega_\varepsilon(x) = 0$. These points are often referred to in the astrophysical literature as the *corotation points* or *Lindblad resonances* of a disk (e.g., Papaloizou & Pringle, 1984). While at first glance it may seem that the corotation points ought to be important to the dynamics investigated here, we find in our results that they in fact play little role. The main reason appears to be because the expressions found in the numerator associated with this term, i.e. $2\Omega_0\alpha\hat{\Pi} + \sigma\partial_x\hat{\Pi}$, always gets nearly as small as the value of the denominator in this region. This would cease to be the case if, for example, self-gravitational physics were included in the analysis. While further elucidation to clarify the inactivity of the Lindblad resonances are surely in order, because these layers play no role in our results these matters are not considered forthwith.

4. CHOICE OF BAROTROPIC VELOCITY PROFILES, SOME NOMENCLATURE

We consider a number of barotropic shear profiles $V_0(x)$ that are departures from pure Keplerian flow. For the work presented here there are three kinds of flow profiles (Figure 1) examined which are frequently identified by the number of "jumps" occurring in the mean vorticity field of the flow:

The vorticity step. This single vorticity jump profile (Figure 1a) , and its derivatives, are given by

$$V_0 = \omega_a \epsilon \ln\left[\cosh\left(\frac{x}{\epsilon}\right)\right],$$
$$V_{0x} = \omega_a \tanh\left(\frac{x}{\epsilon}\right),$$
$$V_{0xx} = \frac{\omega_a}{\epsilon}\mathrm{sech}^2\left(\frac{x}{\epsilon}\right). \qquad (38)$$

The model profile is governed by two parameters, ω_a (units of inverse time) and ϵ (units of length). The latter quantity controls how sharply the shear transition occurs (around x) while the former dictates the shear profile for values of $|x| \gg \epsilon$, i.e. $V_0 \approx \omega_a|x|$ and $V_{0x} \approx \omega_a \mathrm{sgn}(x)$ as $x \to \pm\infty$. The useful feature of this type of model (and for the others described hereafter) is that as $\epsilon \to 0$ the profile resembles a piecewise linear velocity field. In this sense, as $\epsilon \to 0$ $V_{0xx} \approx 2\omega_a\delta(x)$.

The shear layer. The double jump in vorticity is a facsimile of the classic Rayleigh shear profile (Rayleigh, 1880, Drazin & Reid, 1981) in which constant opposite velocity layers sandwich a uniform shear layer of thickness 2Δ centered at $x = 0$. Thus we have

$$V_0 = \frac{\omega_a\epsilon}{2}\left\{\ln\left[\cosh\left(\frac{x-\Delta}{\epsilon}\right)\right] - \ln\left[\cosh\left(\frac{x+\Delta}{\epsilon}\right)\right]\right\},$$
$$V_{0x} = \frac{\omega_a}{2}\left[\tanh\left(\frac{x-\Delta}{\epsilon}\right) - \tanh\left(\frac{x+\Delta}{\epsilon}\right)\right],$$
$$V_{0xx} = \frac{\omega_a}{2\epsilon}\left[\mathrm{sech}^2\left(\frac{x-\Delta}{\epsilon}\right) - \mathrm{sech}^2\left(\frac{x+\Delta}{\epsilon}\right)\right]. \qquad (39)$$

The asymmetric jet. In the absence of a Keplerian shear the triple jump profile described below will physically resemble that of a jet. However, taken in aggregate with the background Keplerian shear, the composite flow describes a shear with a weak jet-like undulation atop of it. Nevertheless, we refer to this as "jet" in so far as the deviation flow V_0 resembles one. The flow V_0 involves three steps in the mean vorticity profile located at positions $-\Delta^-, 0$ and Δ^+. The vorticity of V_0 in both the regions $x > \Delta^+$ and $x < -\Delta^-$ are zero while the vorticity is given (approximately) to be ω_a^- for the region $-\Delta^- < x < 0$ and ω_a^+ for the region $0 < -\Delta^+ < x$. Thus we have

$$V_0 = \frac{\omega_a^-}{2}\epsilon\left\{\ln\left[\cosh\left(\frac{x+\Delta^-}{\epsilon}\right)\right] - \ln\left[\cosh\left(\frac{x}{\epsilon}\right)\right]\right\}$$
$$- \frac{\omega_a^+}{2}\epsilon\left\{\ln\left[\cosh\left(\frac{x-\Delta^+}{\epsilon}\right)\right] - \ln\left[\cosh\left(\frac{x}{\epsilon}\right)\right]\right\}.$$
$$V_{0x} = \frac{\omega_a^-}{2}\left[\tanh\left(\frac{x+\Delta_-}{\epsilon}\right) - \tanh\left(\frac{x}{\epsilon}\right)\right]$$
$$- \frac{\omega_a^+}{2}\left[\tanh\left(\frac{x-\Delta^+}{\epsilon}\right) - \tanh\left(\frac{x}{\epsilon}\right)\right].$$
$$V_{0xx} = \frac{\omega_a^-}{2\epsilon}\left[\mathrm{sech}^2\left(\frac{x+\Delta^-}{\epsilon}\right) - \mathrm{sech}^2\left(\frac{x}{\epsilon}\right)\right]$$
$$- \frac{\omega_a^+}{2\epsilon}\left[\mathrm{sech}^2\left(\frac{x-\Delta^+}{\epsilon}\right) - \mathrm{sech}^2\left(\frac{x}{\epsilon}\right)\right]. \qquad (40)$$

Most of the variation of this mean velocity field is confined to within $-\Delta^- < x < \Delta^+$ centered $x = 0$ and once one has moved sufficiently far from this region the flow returns to being largely Keplerian. For $\omega_a^+ = \omega_a^-$ and $\Delta^+ = \Delta^-$, in the limit $\epsilon \to 0$ the resulting symmetric profile recovers the so-called triangular jet (Drazin, 2002).

We reference the nature of the velocity profile in terms of deviations from the Keplerian state according to the following convention: if $dV_0/dx < 0$ then we say that the profile (or the part under consideration) is *anticyclonic* with respect to the Keplerian shear, while if $dV_0/dx > 0$ then we say that profile (or part under consideration) is similarly *cyclonic*. Often times, we will consider the Rossby number, defined by

$$\mathrm{Ro} \equiv \frac{1}{2\Omega_0}\frac{dV_0}{dx},$$
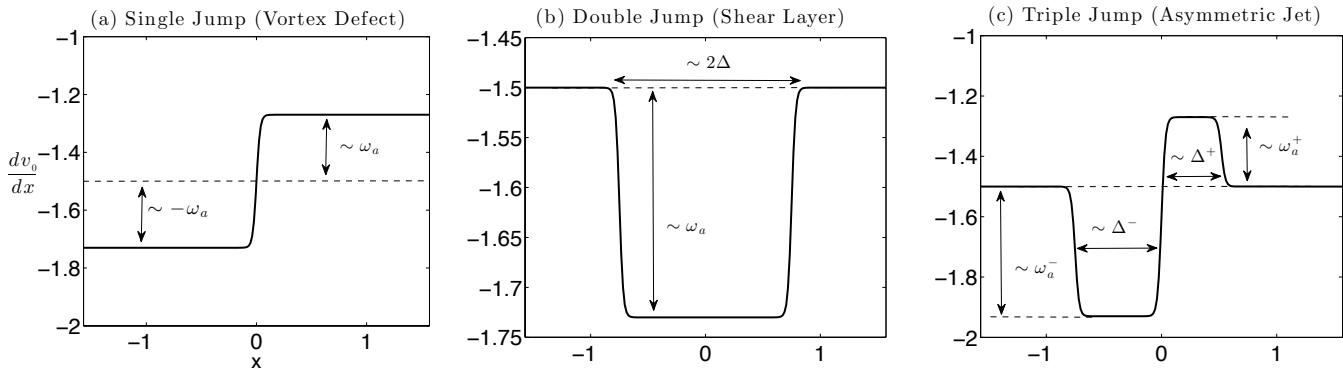
Figure 1. The total shear profile $(dv_0/dx = -3\Omega_0/2 + dV_0/dx)$ of the two barotropic velocity fields detailed in Section 4: (a) The "vortex step", (b) the "shear layer", and (c) the "asymmetric jet". The shear is scaled in units of Ω_0 while the radial length x is scaled to the box scale L. Note that all shear fields shown include the background Keplerian state $(= -3\Omega_0/2)$ which is indicated for reference by the dashed horizontal line in panel (a). The deviation from Keplerian shear profile shown in panel (b) is anti-cyclonic while in panel (c) it is anti-cyclonic in the region $-\Delta^- < x < 0$ provided $\omega_a^- < 0$ and it is cyclonic for $0 < x < \Delta^+$ provided $\omega_a^+ > 0$.

which is the same definition as used by M13 and Marcus et al. (2015). We use Ro to quantify the change of the vorticity in part or in the whole of a profile being tested. For example, the jump in the vorticity across the single step vorticity defect is ω_a while the effective Rossby number characterizing deviations of the shear flow about the Keplerian state is $\text{Ro} = \mathcal{O}\left(|\omega_a|/2\Omega_0\right)$. Generally speaking, jumps in the vorticity relate to the Ro in the way indicated and we think of them in terms of this equivalence hereafter.

5. RELEVANT LENGTH AND TIME SCALES, AND DEPENDENCE OF RESULTS ON PROBLEM PARAMETERS

The linearized equations and the flow fields we have adopted to study are presented in dimensional units mainly in order to facilitate comparison between these theoretical results and numerical results reported in the literature (namely, M13). The shearing box equations are expressed in terms of length scales proportional to the local scale height of the disk (e.g., Umurhan & Regev, 2004). In the absence of any other superimposed flow fields there are no other natural length scales in the problem. Given the aforementioned flow fields described in the previous section, there are now two length scales are introduced to the problem, namely, Δ (or $\Delta^\pm$) and ϵ respectively describing the width(s) of the shear layer (jet flow) and the length scale of their corresponding transition zones.

Similarly, the shearing box equations are generally expressed in time scales proportional to the inverse rotation rate of the disk, Ω_0^{-1}. The plain Coriolis effects (in the absence of any V_0) are expressed in equation (36) as the square of the epicyclic frequency ω_ε^2, which is in units of Ω_0^2. In terms of the shearing box equations utilized in this work, the Brunt-Väisälä frequency $(\sqrt{g\beta})$ is an independent time scale appearing in the system. The addition of the flow fields V_0, discussed in Section 4, introduces additional timescales: $1/\omega_a$ associated with the vorticity step flow and shear layer models or, the two timescales $1/\omega^\pm$ for the jet flow model.

Had we chosen to do so, the governing equations (like, for example, equation 36) would have been non-dimensionalized according to ϵ (spatial scales) and Ω_0^{-1}

(temporal scales). The resulting equations would then transparently exhibit their dependence upon the non-dimensional parameters: $\alpha\epsilon$, $m\epsilon$, $g\beta/\Omega_0^2$ and ω_a/Ω_0. For the vorticity-step model profile calculation, these four parameters completely characterize the system's solutions. The results of shear layer problem depend upon five parameters, i.e., the four parameters of the vorticity-step profile problem with the addition of Δ/ϵ, describing the ratio width of the shear layer to the size of its transition zone. The results for the jet profile are described by seven parameters: $\alpha\epsilon$, $m\epsilon$, $g\beta/\Omega_0^2$, $\Delta^\pm/\epsilon$ and $\omega_a^\pm/\Omega_0$.

We have checked and verified that the numerical results we develop (and describe hereafter), reproduces invariant solutions for invariant values of the aforementioned parameters. For example, for the vorticity-step problem we verify that the eigenvalues we find depend strictly on $m\epsilon$, $\alpha\epsilon$ as well as $g\beta/\Omega_0^2$ and ω_a/Ω_0 only. A variation in ϵ accompanied by adjustments in α and m that leave $m\epsilon$ and $\alpha\epsilon$ invariant leave the results invariant up to numerical accuracy of the computational algorithm.

In more realistic disk models, the Brunt-Väisälä frequency is a function of vertical position. Indeed, the vertical component of gravity has the approximate local dependence $g \sim \Omega_0^2 z$. Buoyancy, which is a non-dimensional quantity, is best gauged by the vertical entropy profile which, in turn, is strongly dependent on the global disk model under consideration. Provided the entropy structure is stably stratified and symmetric with respect to the disk midplane, we suppose that the vertical gradient of buoyancy $\beta \sim z/(HH_\beta)$, in which H_β is the vertical variation scale of the (non-dimensionalized) entropy while H is the usual pressure scale-height. Supposing the model dependent $H_\beta \sim \mathcal{O}(H)$, then the square of the Brunt-Väisälä frequency takes on the range of values given by the relationship: $g\beta \approx \Omega_0^2(z/H)^2$. Considering that the shearing box equations are formally valid to a few scale heights above the disk midplane, and since our model formulation assumes constant values of $g\beta$, we make sure to consider values of $0 < g\beta \leq 6\Omega_0^2$, in which the upper bound corresponding to about 2.5 disk scale heights while the lower bound corresponds to locations in the vicinity of the disk midplane.

6. SOLUTION METHOD

We solve the coupled integral equations (17–19) assuming normal mode perturbations of the form

$$\begin{pmatrix} \zeta'(x,t) \\ D'(x,t) \\ \theta'(x,t) \end{pmatrix} = \begin{pmatrix} \hat{\zeta}(x) \\ \hat{D}(x) \\ \hat{\theta}(x) \end{pmatrix} e^{-i\omega t} + \text{c.c.} \qquad (41)$$

together with the corresponding Green's function solutions for the diagnostic relationships ϕ, ψ' and Π' found in equations (21) and (24). As noted earlier, we seek solutions that show exponential decay as $|x| \gg 1$ which necessarily precludes simple wave normal mode solutions that have no attenuation in the far limit.

The system is a series of three coupled integral equations. The variables, ζ, D and θ, are discretized on either a uniform or Gaussian grid x_j of N points, but for the purposes of this report we quote the results developed using a uniform grid only. [6] Thus each variable is numerically represented as a column vector corresponding to its values on the grid, i.e. $\hat{\zeta} \mapsto \zeta_j, \hat{D} \mapsto D_j$ and $\hat{\theta} \mapsto \theta_j$. The Green's functions are turned into matrix operators so that, for instance, the stream function $(\hat{\psi} \mapsto \psi_j)$ is written as a matrix operation relating it to the vertical vorticity, that is to say

$$\psi_j = \mathbf{G}_{jn}^{(\psi)} \otimes \zeta_n, \qquad \mathbf{G}_{jn}^{(\psi)} \equiv -\frac{dx}{2\alpha} e^{-\alpha|x_j - x_n|},$$

where dx is the grid spacing and the symbol $\otimes$ is the matrix multiplication operation. The corresponding derivative of $d\hat{\psi}/dx \mapsto \left(d\psi\right)_j$ is written as

$$\left(d\psi\right)_j = \mathbf{dG}_{jn}^{(\psi)} \otimes \zeta_n,$$

in which

$$\mathbf{dG}_{jn}^{(\psi)} \equiv \frac{dx}{2} \text{sgn}(x_j - x_n) e^{-\alpha|x_j - x_n|}.$$

A similar set of matrix operations are defined and implemented for the potential function $\hat{\phi} \mapsto \phi_j$ and the pressure field $\hat{\Pi} \mapsto \Pi_j$. In this construction, the exponential decay of solutions as $|x| \to \infty$ is ensured. The complete set of equations (17–19) is converted into a single matrix form

$$\frac{\partial \mathbf{V}}{\partial t} = \mathbf{M} \otimes \mathbf{V} \qquad (42)$$

with

$$\mathbf{V} = \left(\zeta_1, \cdots, \zeta_j, \cdots, \zeta_N, D_1, \cdots, D_N, \theta_1, \cdots, \theta_N\right)^{\mathsf{T}}. \qquad (43)$$

Assumption of the normal mode form in equation (41) turns the above into a single matrix problem to determine the unknown eigenvalues $-i\omega$. $\mathbf{M}$ is constructed following the method described in Umurhan (2010).

We then go through two stages to obtain a solution. *Stage 1* uses standard matrix inversion methods to establish both eigenvalues and the corresponding eigenfunctions. Because the method is computationally expensive,

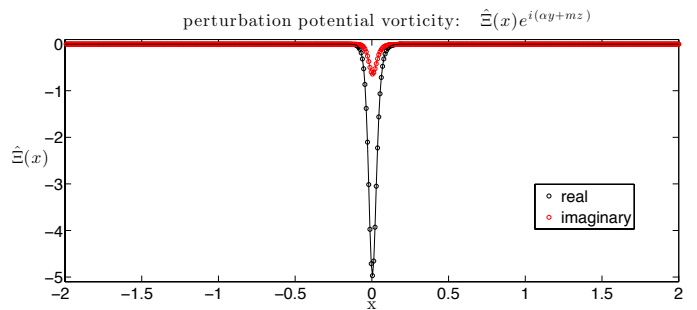[6] All solutions obtained and reported herein are equivalently obtained using either discretization.

Figure 2. Potential vorticity for the problem relating to the previous two figures. The potential vorticity Ξ' is based on its definition in equation (25). Most power in this quantity is contained mainly in the region surrounding $x = 0$ corresponding to the maximum of the mean vorticity gradient. There is no discernible power near the critical points $x_{bg}^{\pm}$ - as expected.

we often use this method to determine the approximate solution on a coarse grid and then we refine this same solution through *Stage 2*: which interpolates the solution onto a finer grid (either 2 or 4 times) and then solves the discretized system matrix operator system using a standard Newton-Raphson-Kantorovich solution technique.

The benefit of this approach is that Stage 1 produces all of the normal modes permitted by the system and Stage 2 helps to identify which of the numerically determined solutions are spurious and which are robust. Spurious solutions are identified as those candidate normal mode solutions whose eigenvalues show no convergence with increased resolution. Z-modes are found to be particularly tricky to obtain reliably, generally requiring anywhere from 700-1500 grid points of radial resolution on domains ranging from π to 2π.

7. LINEAR THEORY RESULTS

We have scanned for solutions in the event that the basic flow is a pure Keplerian velocity field, i.e. for $V(x) = 0$. We find no converged continuous normal modes. The reason appears to us clear: the structure of the alternative formulation of the equations, i.e. (26–28) together with $\Xi' = 0$ indicates that the system supports shear modified inertial-gravity waves. No normal modes are expected since the radial extent of the system is infinite and, as such, is unable to support a "global" supported mode. Normal modes are potentially possible only if other boundary conditions are adopted (not done here). Of course, as an initial value problem with a given initial disturbance, this system would respond by shedding inertia-gravity waves which are non-normal mode solutions of (26–28). These waves would propagate out to $x \to \pm\infty$, but they do not qualify as normal modes in this case.

Normal modes do exist for $V_0(x) \neq 0$. In this case, there are two kinds of modes supported which we henceforth refer to as "Rossby modes"(R-modes) and "zombie modes" (Z-modes). The R-modes are the three-dimensional continuation of the classical two-dimensional shear modes examined in the literature (e.g. the Rayleigh shear layer, the RWI,the triangular jet, etc.). R-modes are unstable when two or more Rossby waves (sometimes known as "Rossby edge waves"), each being associated with local extrema in the radial vorticity gradient of the basic shear flow, become resonantly phase-locked due
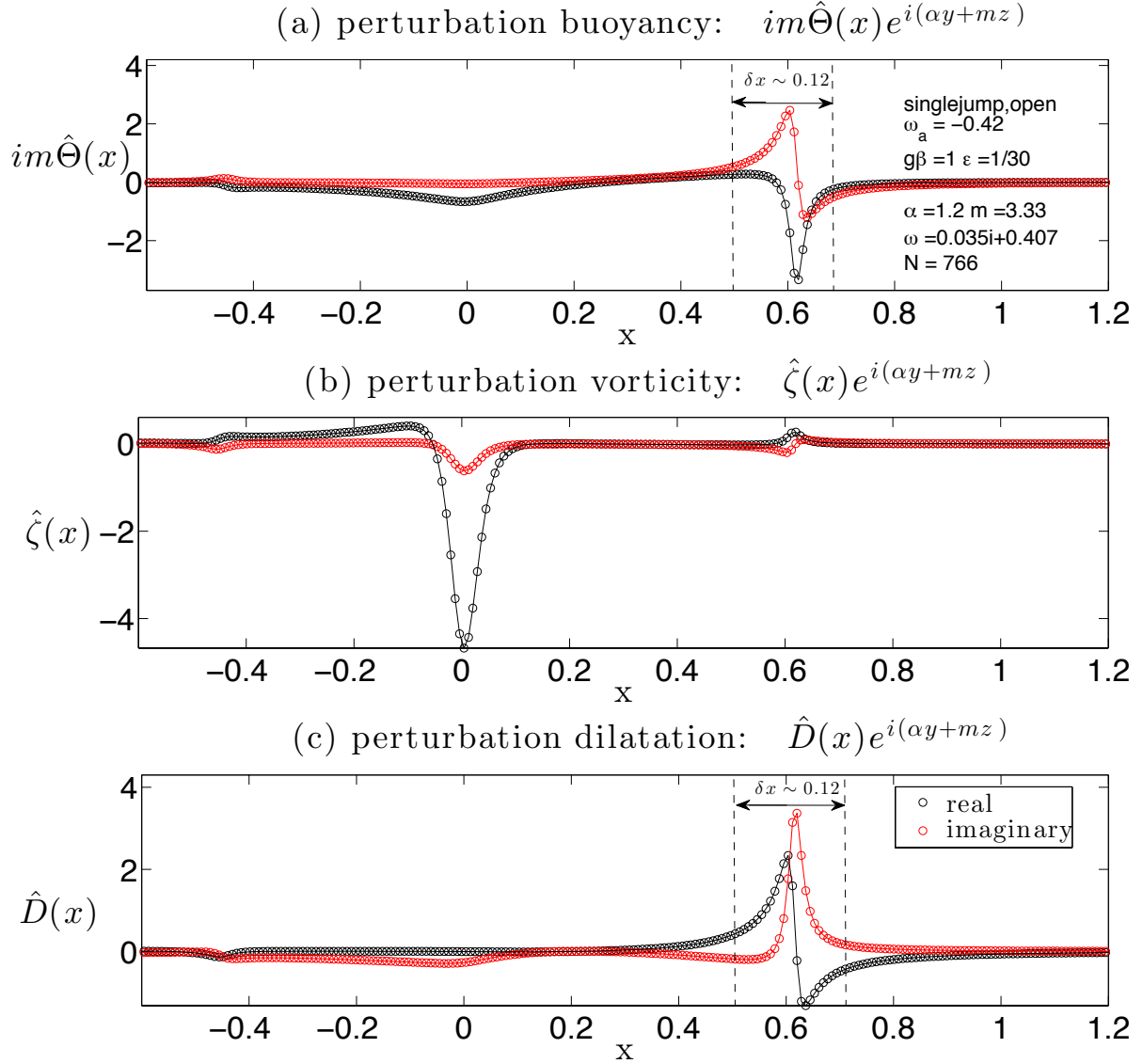
(a) perturbation buoyancy: $im\hat{\Theta}(x)e^{i(\alpha y + mz)}$

(b) perturbation vorticity: $\hat{\zeta}(x)e^{i(\alpha y + mz)}$

(c) perturbation dilatation: $\hat{D}(x)e^{i(\alpha y + mz)}$

Figure 3. Array of Z-mode eigenmodes for the vorticity step problem: $g\beta = 1.0\Omega_0^2$, $\omega_a = -0.42\Omega_0$, $\alpha = 1.2$ and $m = 3.33$ with $\epsilon = 1/30$. This sample flow field has an equivalent deviation flow field with Ro= 0.21. The panels show the perturbation fields for (a) the buoyancy (b) the vorticity, (c) the dilatation. The basic state vorticity gradient appears imprinted in the perturbation vorticity field around $x = 0$. The induced critical layers appearing at $x_{bg}^{\pm} \approx -0.45, 0.62$ are most prominent in the buoyancy and dilatation fields. Numerical details: linear grid used is $N = 766$ with solutions shown by open circles with a fitted curve connecting them. Solutions calculated on the domain $-\pi < x < \pi$, however only the active parts are shown in the figure.

to their mutual interaction, i.e., the counter propagating Rossby wave mechanism (Baines & Mitsudera 1994; Heifetz et al. 1999; **?**). There are no unstable R-modes in the single vorticity step flow field because it can support only a single Rossby wave precluding the possibility of resonant wave-wave interaction.

On the other hand, the Z-modes are different from the R-modes in that instability in these modes involves the resonant interaction between a single Rossby wave and a buoyant critical layer(s) nearby. In the following subsections we examine the properties of Z-modes for the three model shear flows.

7.1. Z-modes in the vorticity step model

The velocity shear field given in equation (38) can support a single localized Rossby edge wave that propagates along the azimuthal direction. The core of the wave is localized around $x = 0$ as this is the location where the radial gradient of the basic state shear profile is the greatest. In the limit where $m\epsilon \to 0$, together with $m \ll \alpha$, this disturbance can be thought of as a vertically uniform azimuthally propagating edge wave and it was demonstrated in Umurhan (2010) to have a real frequency given by $\omega = \omega_a$ in the effective limit $\alpha\epsilon \to 0$ (α fixed, $\epsilon \to 0$). The frequency response of the unstable modes reported here are very nearly equal to this value, i.e. $\text{Re}(\omega) \approx \omega_a$ - and this is especially true for modes with values of $m \le 2$ (see Figure 5). *We consider this Rossby edge wave to be*
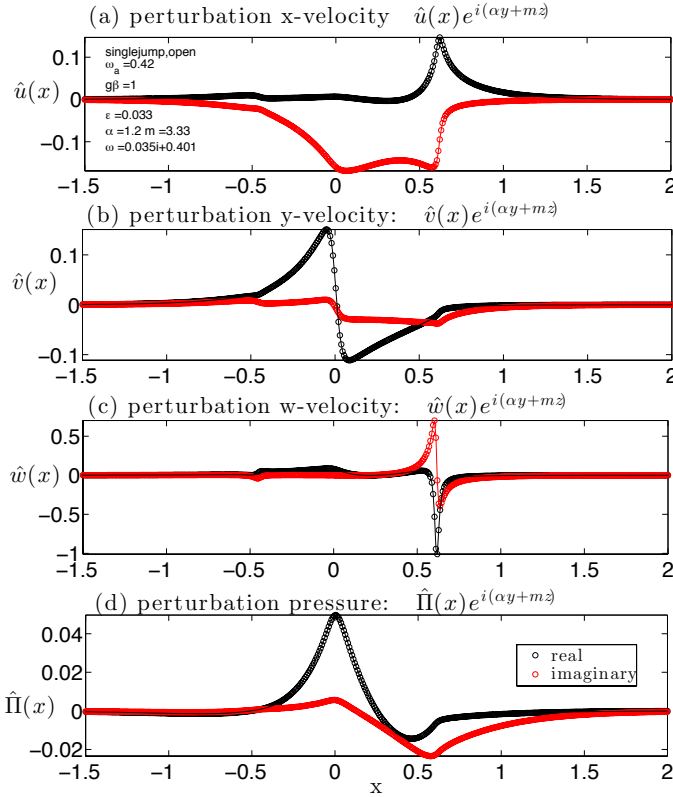
(a) perturbation x-velocity $\hat{u}(x)e^{i(\alpha y + mz)}$

(b) perturbation y-velocity: $\hat{v}(x)e^{i(\alpha y + mz)}$

(c) perturbation w-velocity: $\hat{w}(x)e^{i(\alpha y + mz)}$

(d) perturbation pressure: $\hat{\Pi}(x)e^{i(\alpha y + mz)}$

Figure 4. Like the previous figure but showing the fields (a) u', (b) v', (b) w' and (d) Π'. All quantities show substantial drop-off as x approaches the left and right boundaries emphasizing the strong localized nature of these disturbances. We emphasize that the solutions are calculated on the domain $|x| < \pi$ but that for purposes of clarity only the inner portions are displayed since all solutions show exponential decay with increased $|x|$.

the basic carrier mode of the instability associated with Z-modes.

With this insight, we can predict the approximate locations of the various critical layers in the limit where both m is relatively small and $\epsilon \ll 1$.[7] For the classical shear critical layer we have $\alpha v_0(x_{pp}) - \mathrm{Re}(\omega) = 0$, which after a little manipulation becomes

$$x_{pp} \approx \left(\frac{1}{\alpha}\right)\left(\frac{\omega_a}{-3\Omega_0/2 + \omega_a \mathrm{sgn}\left(x_{pp}\right)}\right). \qquad (44)$$

Similarly, the critical layers associated with gravity effects, i.e. those points $\alpha v_0(x_{bg}^\pm) \pm \sqrt{g\beta} - \mathrm{Re}(\omega) = 0$ are given by

$$x_{bg}^\pm \approx \left(\frac{1}{\alpha}\right)\left(\frac{\omega_a \pm \sqrt{g\beta}}{-3\Omega_0/2 + \omega_a \mathrm{sgn}\left(x_{bg}^\pm\right)}\right). \qquad (45)$$

The above are rough guides – in actuality the position of the critical layers will differ from the above approximate form when $m \gg 1$, since ω of the Rossby wave is no longer expected to be given by ω_a. Nonetheless, when the correct value of $\mathrm{Re}(\omega)$ appropriate for the given Rossby

---

[7] We also note that in this sense we consider ϵ to be sufficiently small if its value is below any numerically resolvable grid scale length.

---

wave is input, we obtain the correct critical layer position as expected.

The perturbation potential vorticity is displayed in Figure 2. Consistent with our analysis of Section 3.1, we see that Ξ' has power purely in the region of $x = 0$ and no discernible power in the regions around the critical points $x_{bg}^\pm$. This is rationalized because the potential vorticity is (linearly) forced only by the advection of the mean vorticity gradient which has appreciable power only around $x = 0$. For us, this observation lends further credence to our claim that the main perturbation structure is that of a Rossby wave and that it is this wave that triggers the critical layers at $x_{bg}^\pm$.

In Figure 3 we show a fairly typical result involving unstable modes of the system. The three panels show the quantities θ', ζ' and D'. The vorticity shows strong power near $x = 0$. This arises from the radial transport of the mean vorticity gradient term $u' \cdot v_{0xx}$ and indicates that the perturbation is structurally that of a Rossby wave centered at that position. According to equation (45) and given the parameters of the system, the positions of the two buoyant gravity wave critical layers are $x_{bg}^- \approx -0.448$ and $x_{bg}^+ \approx 0.616$. The importance of these locations are self-evident in both the buoyancy and dilatation fields, demonstrating amplified power in the vicinity of those critical layers.

The corresponding perturbation velocity fields and pressure fluctuations are shown in Figure 4, indicating the strong localized nature of the disturbances where the amplitude of the perturbations decays to zero rapidly as $|x| \gg \epsilon$ (at least, several 100 times ϵ). It is generally for this reason we are confident that these responses (and overall physical effects) are independent of the assumed radial boundary conditions so long as the boundaries are set far enough away. We have scanned the response of this system using both impenetrable walls and periodic conditions in the radial direction and we find that the response is essentially the same so long as the boundaries themselves are set far enough apart. In principle this means L being sufficiently greater than π, but in practice we find that even slightly larger than $L = \pi$ is good enough. Observable signatures of the critical layers at $x = x_{bg}^\pm$ are also evident in these fields, however, it is most prominent in the vertical velocity. This has profound implications for nonlinear driving (Section 8).

The sizes of the critical layers scale approximately as $\sim \sqrt{\mathrm{Im}(\omega)/\Omega_0}/m$. This fact can be seen from an elementary boundary layer scaling analysis of Eq. (36) in the vicinity of $x = x_{bg}$. [For an analogous critical layer analysis see the thorough examination of a barotropic jet instability performed by Balmforth and Piccolo (2001)]. The critical layer arises from the first term on the RHS of equation Eq. (36), and when the layer is activated, this term balances the second x derivative of $\hat{\Pi}$:

$$\partial_x^2 \hat{\Pi} \approx \frac{\omega_\varepsilon^2 - g\beta}{\left(\sqrt{g\beta} - \alpha v_0(x) + \omega\right)\left(\sqrt{g\beta} + \alpha v_0(x) - \omega\right)} m^2 \hat{\Pi}. \qquad (46)$$

in which we have explicitly factored the denominator of the term on the RHS of the above expression. For a given solution value ω, at the critical layer we have according

to equation (37),

$$\sqrt{g\beta} \pm \left[\alpha v_0(x_{\mathrm{bg}}) - \mathrm{Re}(\omega)\right] = 0,$$

A first order Taylor series expansion of the term $\alpha v_0(x)$ near $x = x_{\mathrm{bg}}$ produces

$$\alpha v_0(x) \approx \alpha v_0(x_{\mathrm{bg}}) + \alpha \left.\frac{dv_0}{dx}\right|_{x_{\mathrm{bg}}} (x - x_{\mathrm{bg}})$$

Considering the assumption $|\mathrm{Im}(\omega)| \ll |\mathrm{Re}(\omega)||$ (noting that all of the growth rates determined in this study usually a factor of 10 smaller than Ω_0), putting all of the above approximate forms into Eq. (46) reveals

$$\partial_x^2 \hat{\Pi} \approx \frac{\left[\omega_\varepsilon^2(x_{\mathrm{bg}}) - g\beta\right] m^2}{2\sqrt{g\beta}\left[\alpha \left.\frac{dv_0}{dx}\right|_{x_{\mathrm{bg}}} (x - x_{\mathrm{bg}}) - i\mathrm{Im}(\omega)\right]} \hat{\Pi}. \quad (47)$$

For $\mathrm{Im}(\omega) \neq 0$, the rate of change of the second derivative of $\hat{\Pi}$ is scaled by the value of the coefficient on the RHS of Eq. (47) evaluated at $x = x_{\mathrm{bg}}$. [8] Thus, we have in the region very near $x \approx x_{\mathrm{bg}}$,

$$\partial_x^2 \hat{\Pi} \approx i\frac{1}{\Gamma^2}\hat{\Pi}, \qquad \Gamma^2 \equiv \frac{2\sqrt{g\beta} \cdot \mathrm{Im}(\omega)}{\left[\omega_\varepsilon^2(x_{\mathrm{bg}}) - g\beta\right] m^2}. \quad (48)$$

The magnitude of Γ sets the approximate variation scale of the boundary layer region. For the solutions shown in figures (3–4), we have indicated with hatched vertical lines the regions in which the critical layer is most obvious (see also Figure 13). The width of the region, which we designate by δx, should be approximately twice the value of $|\Gamma|$ predicted by the above analysis (48). For the critical layer near $x = 0.62$, we predict values of $\Gamma \sim 0.0575$ based on the input parameters, while we see that the width of the buoyant critical layer zone in these figures is about $\delta x \sim 0.12$.

The boundary layer scaling for the buoyant critical layers developed here is generally valid for the results of the other two model flows discussed in Sections 7.2 and 7.3.

We have also verified that the main trend predicted by (48) holds, namely that for all other parameters equal, the boundary layer regions shrinks in proportion to $\sqrt{|\mathrm{Im}(\omega)|}/m$. This last observation explains why it becomes increasingly more difficult to ascertain resolved solutions as m increases.

In Figure 5 we show growth rates as a function of the vertical wavenumber m. The plots are fairly typical of the responses of the system when unstable. Keeping the azimuthal wavenumber fixed around $\alpha \approx 1.2$, we see that the unstable vertical wave numbers will span a finite range with a corresponding peak growth rate. Normal modes appear in stable/unstable pairs. In this single step vorticity model, growth occurs irrespective of the sign of ω_a. For example, for values of $|\omega_\alpha| \approx 0.43\Omega_0$ (Ro ≈ 0.23) together with $g\beta = 1.2\Omega_0^2$, the maximum growth rate occurs around $m = 3.5$ and has a growth $\mathrm{Im}(\omega) \approx 0.045\Omega_0$

indicating that for this value of Ro, the e-folding time of growth is 3-4 rotation times, i.e., $\sim \mathcal{O}\left(1/2\pi\mathrm{Im}(\omega)\right)$.

The maximum growth rate and corresponding vertical wavenumber of maximal growth decreases as $|\omega_a|$ decreases. Furthermore, for $g\beta = 1.0\Omega_0^2$ we find that if $|\omega_a| < 0.2\Omega_0$ there appears to be no instability at all. This criterion roughly corresponds to the Ro of the vorticity step necessarily being less than 0.1 for the system to be stable. This is determined based on our highest resolution examinations. Lower values of Ro may also be unstable, but they are not currently resolvable in our searches.

7.2. Shear Layer
7.2.1. *R-modes*

In this subsection as well as in Section 7.3.1 we study the evolution of perturbations with no vertical dependence ($m = 0$). In that case the horizontal divergence $D' = 0$ and we only have to solve the normal mode version of equation (27)

$$\left[-i\omega + i\alpha\left(-1.5\Omega_0 x + V_0(x)\right)\right]\hat{\zeta} = V_{0xx}\hat{u} \quad (49)$$

where the vertical vorticity and corresponding horizontal velocity fields are related to the normal mode streamfunction $\hat{\psi}(x)$ more simply via

$$\zeta = \frac{d^2\hat{\psi}}{dx^2} - \alpha^2\hat{\psi}, \qquad \hat{v} = -\frac{d\hat{\psi}}{dx}, \quad \hat{u} = -i\alpha\hat{\psi}. \quad (50)$$

This is essentially an analysis of the RWI except for a system with two local extrema in the pressure profile (whereas the usual RWI is an analysis of a configuration with only one local pressure extremum). This analysis of the barotropic shear layer model gets simplified if we implement the strategy used in Umurhan (2010), wherein $\epsilon \to 0$ is assumed. In this limit, the continuous shear layer flow profile becomes an analytically tractable problem comprising of three piecewise linear shear profiles. The solution procedure follows the steps detailed in Appendix A relating to the same type of analysis done on the asymmetric jet (examined in the next section). [9] For the shear layer considered here it is a slight generalization of Rayleigh's shear layer analysis (Rayleigh, 1880) with the additional superposition of the background Keplerian shear profile. The resulting frequency response is given by

$$4\omega^2 = \omega_a^2 e^{-4\alpha\Delta} - \left[3\alpha\Delta\Omega_0 + (1 - 2\alpha\Delta)\omega_a\right]^2. \quad (51)$$

Inspection shows that this system becomes unstable when ω goes through zero. The physical condition for instability is the phase locking of two counterpropagating Rossby waves (Baines & Mitsudera 1994; Heifetz et al. 1999). By setting $\omega = 0$ we find the condition for

---

[8] The technical reason for this is that the branchcut of both the above ordinary differential equation and its associated solution lies along one of the two imaginary axis on the complex plane of the function $\chi \equiv x - x_{\mathrm{bg}}$.

[9] It ought to be noted that there are subtleties introduced because of the use of piecewise linear profiles, for instance, it is sometimes the case that piecewise linear profiles predict modes that do necessarily have counterparts in analysis of flow profiles that are infinitely differentiable. The normal modes generated herein, through the use of these piecewise linear representations, all have counterpart modes in their corresponding infinitely differentiable flow profiles.
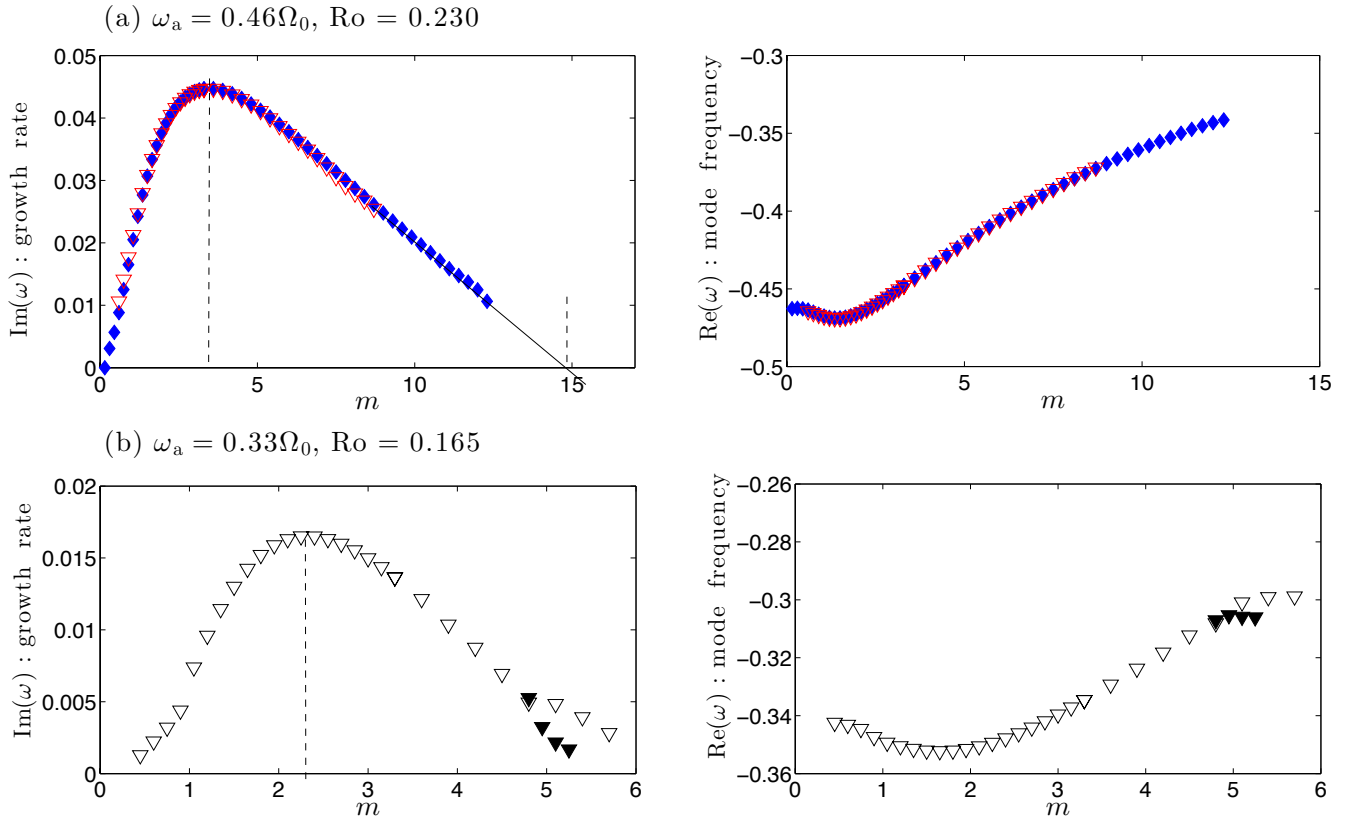
(a) $\omega_{\mathrm{a}} = 0.46\Omega_0$, Ro = 0.230

(b) $\omega_{\mathrm{a}} = 0.33\Omega_0$, Ro = 0.165

Figure 5. Z-mode growth rates and frequencies as a function of vertical wavenumber m for two different values of ω_a in the vorticity step profile (all rates expressed in units of Ω_0): (a) $\omega_a = 0.46$ (b) $\omega_a = 0.33$. Other parameters shared by both examples: $g\beta = 1.2, \alpha = 1.1$ with $\epsilon = 0.05$. Peak growth rates and their corresponding values of m are denoted with dashed vertical lines. General pattern indicated is that as ω_a gets smaller the wavenumber range (in m) and maximum growth rate diminish. The growth rates in panel (a) were determined on a domain $-L < x < L$ where $L = \pi$ (blue-filled diamonds) and $L = 2\pi$ (upside-down red triangles). Each was done with the same number of Chebyshev grid points $N = 1461$. Note that as $|\mathrm{Im}(\omega)|$ gets sufficiently small ($\sim 2L/N$) reliably converged solutions become more difficult to determine, necessitating more resolution. The fitted curve (black line), extrapolating the growth rate as m increases, shows that $m_{\max} \approx 14.5$. In panel (b) the calculation was done on $L = \pi$ but for two different resolutions. The filled black triangles are for $N = 2301$ while $N = 1461$ is shown with open black triangles.

marginal growth to be given by

$$\frac{\omega_R^{\pm}}{\Omega_0} = \frac{3\alpha\Delta}{2\alpha\Delta - 1 \pm e^{-2\alpha\Delta}}, \tag{52}$$

where $\omega_R^{\pm}$ is the shear layer amplitude corresponding to marginality. We do not consider the positive roots, ω_R^+, because these generally correspond to composite flows that are strongly cyclonic, i.e., flows in which $dv/dx = -3\Omega_0/2 + \omega_R^+ > 0$ while the negative root, on the other hand, often corresponds to anti-cylonic shear profiles. [10]

If we consider the setting examined in M13, we suppose that the smallest azimuthal wavenumber is the one fitting the box considered therein. The corresponding azimuthal length scale in their box units is approximately $L = (3/2)\pi$. This corresponds to a fundamental azimuthal wavenumber $\alpha = 2\pi/L = 4/3$. Similarly, the width of the shear line-charge is approximately 0.28 (also in their code units). Translating this into our setup, the total width is 2Δ, thus we adopt a value of $\Delta = 0.14$. In this case, the corresponding critical value of ω_a for the R-mode is given from Eq. (52) by $\omega_R^- \approx -0.426\Omega_0$,

---

[10] This is generally true upon examination of the marginal condition in Eq. (52.

with a corresponding critical Rossby number of Ro = $|\omega_R^-/2\Omega_0| \approx 0.213$. Values of $0 > \omega_a > \omega_R^-$ should then be stable to the RWI. We find that the value of ω_R^- predicted in Eq. (52) generally predicts more negative values of ω_R^- that are borne out in our models. The reason for this is that we adopt non-zero values of ϵ (= 1/50) for all the models reported in this section. The discrepency is generally 2-5 % the predicted values. [11]

7.2.2. *Z-modes*

The results of the vortex-step profile indicates that Z-modes ought to be present, especially for conditions in which $\omega_a > \omega_R^-$ and we accordingly scan the response of the system for these parameter values and assess the instability in ω_a. The results reported in M13 suggest that the Z-mode is strong and expressed for values of Ro ≈ 0.2, which is slightly lower than the critical value of

---

[11] We have separately checked (but have not included in this manuscript) and verified that as $\epsilon \to 0$ the model value ω_R^- converges to the one predicted for $\epsilon = 0$. Since smaller values of the ϵ parameter requires more grid points to resolve, we have adopted the value chosen here because it minimizes the number of computations required to assess a stable numerical solution while remaining close to the idealized $\epsilon = 0$ model developed earlier.
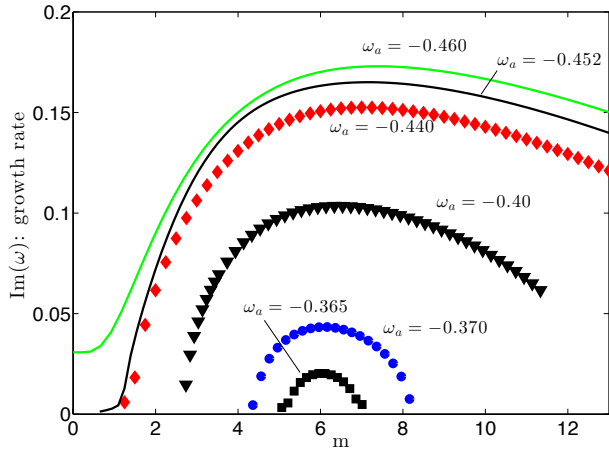
Figure 6. Growth rates (in units of Ω_0) versus vertical wavenumber m for the shear layer profile: $\epsilon = 0.02, g\beta = 4\Omega_0^2, \Delta = 0.142$ and $\alpha = 1.4$. Several different values of the shear layer amplitude are shown in plot scaled by Ω_0. In the model flows used for these plots, the onset of RWI occurs for $\omega_a = \omega_R^- \approx -0.4525\Omega_0$. All basic flows shown are anticyclonic compared to the background shear.

the Rossby number determined above for the activation of R-modes (i.e., Ro ≈ 0.213). Indeed, we find that the Z-mode is recovered in this model in the absence of R-modes. We describe this in the following.

Provided the Brunt-Väisälä frequency $\sqrt{g\beta}$ exceeds some minimum value, Z-modes manifest themselves for shear layer amplitudes, $\omega_a < \omega_z$, where $\omega_z = \omega_z(\alpha\Delta, g\beta)$ is the critical value of the jet's vorticity amplitude in order for Z-modes to appear. As indicated, ω_z is a function of both the square of the Brunt-Väisälä frequency and the relative measure of the jet-width to the azimuthal perturbation length scale. Furthermore, for a given values of $\alpha\Delta$, there are values of $g\beta > N_{crit}^2(\alpha\Delta)$ for which Z-modes *with buoyant critical layers lying outside of the primary shear layer* are present in the absence of the RWI, that is to say, "naked" Z-modes with external critical layers are observed for shear flow amplitudes falling within the range $\omega_R^- < \omega_a < \omega_z$.

Given the symmetry of the shear layer, we find that all Z-modes are unstable with zero oscillatory part in their growth rates. In Figure 6 we show growth rates versus the vertical wavenumbers m for given values of $\alpha\Delta$ and $g\beta$. In this figure, several profiles are shown for differing values of the shear amplitude ω_a. In the particular example displayed, the critical value of ω_z is greater than ω_R^-, which means that for values of $\omega_R^- < \omega_a < \omega_z$ Z-modes are manifested in the models and are naked indeed. For values of $\omega_a < \omega_R^-$ both Z-modes and R-modes are present.

In Figure 7 we show growth rates versus m for fixed values of α, Δ and ω_a for several values of the transition scale ϵ. This figure indicates that for all other parameters held fixed, there exists a value of ϵ – and hence, the ratio Δ/ϵ – for which growth is optimal. We also note that the effect persists even as ϵ gets to be nearly the same order as Δ (i.e, $\Delta/\epsilon \sim 1$), although the growth rates are generally far weaker than they are for optimal conditions. In the example shown in Figure 7, those optimal conditions are $\Delta/\epsilon \sim 3$.
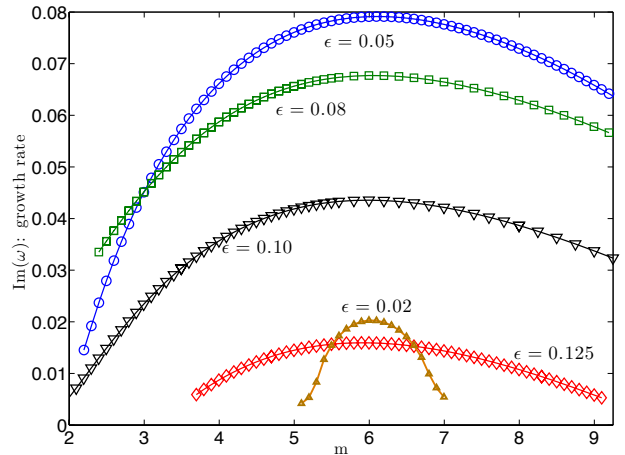

Figure 7. Growth rates (in units of Ω_0) versus vertical wavenumber m for the shear layer profile: $\omega_a = -0.365, g\beta/\Omega_0^2 = 4, \Delta = 0.142$ and $\alpha = 1.4$. Shown on figure are several different values of ϵ. For all other parameters held fixed, the figure indicates that there is an optimal value of ϵ for maximal growth – for the parameter combination considered here $\epsilon \sim 0.05$.

Given that ω has zero real part, one might approximate the critical value of $\sqrt{g\beta}$ in which x_{bg} coincides with Δ. Setting $\omega = 0$ and replacing x_{bg} by Δ in Eq. (37), followed by focusing on the positive root we find the following approximate rule-of-thumb,

$$N_{crit} \equiv \left(\sqrt{g\beta}\right)_c \approx \alpha\Delta\left(-\frac{3}{2}\Omega_0 + \omega_a\right) \qquad (53)$$

where N_{crit} is the critical value. The pattern in the data suggest that this value is in the vicinity of $\omega_a = \omega_R^-$. This is better borne out by the data in what follows.

For example M13 adopted a value of the Brunt-Väisälä frequency $= 2\Omega_0$. In our parameter settings this means choosing $g\beta = 4\Omega_0^2$. In the following example, we consider a model result similar to theirs by adopting a value $\alpha = 1.4$ (slightly larger than their value of $\alpha = 4/3$). According to Eq. (52) this corresponds to $\omega_R^- \approx -0.4655$ while we find in our numerical model flows, with $\epsilon = 1/50$, ω_R^-(model) ≈ -0.4525 (see previous subsection).

Furthermore, using these values in (53) we see that the critical value N_{crit}^2 is approximately $0.15\Omega_0^2$. An examination of the properties of the eigenmodes is consistent with this picture: for values of $g\beta > N_{crit}^2$ Z-mode critical layers appear outside the shear layer. For shear layer amplitudes satisfying $\omega_R^- < \omega_a < \omega_z$, Z-modes are naked.

In Figure 8 we display the critical values $\omega_a = \omega_z$ as a function of $g\beta$ for fixed values of the product $\alpha\Delta$. The value of ω_z is a minimum in the near vicinity of $g\beta = N_{crit}^2 \approx 0.15\Omega_0^2$. For values of $g\beta > N_c^2$ the critical layers appear well outside the shear layer (Figure 9a). For values of $g\beta < N_{crit}^2$ the critical layers appear within the shear layer (Figure 9b). Once again, assuming $\omega = 0$ and assuming α, ω_a fixed, it follows from Eq. (37) that lowering $g\beta$ means shifting the critical layer x_{bg} toward $x = 0$. It is also remarkable that the instability continues on into the limit $g\beta \rightarrow 0$ which suggests that an analytical boundary layer analysis is feasible in this limit (not done here).
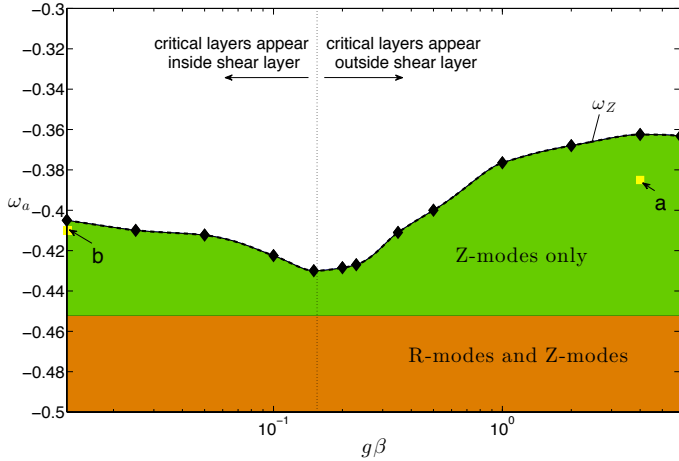
Lastly, in Figure 10 we show the vertical wavenumber

Figure 8. Value of ω_z versus $g\beta$ for fixed value of $\alpha = 1.4$ and $\Delta = 0.14$ (box size $L = 2\pi$, $g\beta$ scaled by Ω_0^2, all rates in units of Ω_0). Diamonds denote numerical values determined while the dashed line is a fit to those values. Numerically determined value of $\omega_R^- \approx -0.453$ denotes transition into R-mode instability. Values of ω_a corresponding to naked Z-modes designated by the green shaded region while values of ω_a for which both Z-modes and R-modes are expressed denoted by the orange shaded region. Vertical dotted line represents the value of of $g\beta = N_{\text{crit}}^2 \approx 0.15$ in which the critical layers correspond to the edges of the shear layer.

m as a function of the Brunt-Väisälä frequency $g\beta$ at which the unstable Z-mode first appears (at $\omega_a = \omega_z$). This value of m generally corresponds to the fastest growing mode as $\omega_a < \omega_z$. This critical vertical wavenumber begins to increase significantly once $g\beta$ increases past N_c^2.

7.3. Asymmetric Jet

7.3.1. R-modes in the asymmetric jet model - the RWI

In this and in the next subsection we consider asymmetric jet profiles that have zero total integrated deviation vorticity. In other words, in considering the flow field given in equation (40) we constrain our parameter variations such that $\omega_a^+ \Delta^+ + \omega_a^- \Delta^- = 0$. In our considerations we keep the ratio $\Delta^-/\Delta^+ \equiv \delta$ fixed which means that ω_a^- is always set according to

$$\omega_a^- = -\omega_a^+ \frac{\Delta^+}{\Delta^-} = -\frac{\omega_a^+}{\delta}. \tag{54}$$

Since the only length scales in this system are given width parameters $\Delta^\pm$, the general response is a function of $\alpha\Delta^+$ and ω^+ for fixed values of δ. The analysis of the system produces the following cubic equation for the value of the eigenvalue ω

$$\omega^3 + a\omega^2 + b\omega + c = 0, \tag{55}$$

in which the coefficients $a = a(\alpha\Delta^+, \omega^+, \delta)$, $b = b(\alpha\Delta^+, \omega^+, \delta)$ and $c = c(\alpha\Delta^+, \omega^+, \delta)$ are real and whose values are detailed in Appendix A. Cubic equations like the one above with real coefficients have two possible kinds of solutions either (i) three real distinct values of ω or (ii) one real and a complex conjugate pair of solutions ω. The physical correspondence is similar to the analysis and conclusions drawn from the simpler RWI setup in Umurhan (2010): when separated Rossby waves interact with one another at a distance, they can become

unstable if their wave speeds become equal and opposite to one another in some reference frame. The same interpretation therefore holds for this jet system as well.

Figure 11 depicts a typical profile of the stability boundaries and growth rates associated with this system for a fixed value of $\delta \approx 1.54$. The pattern of the solutions indicate similarity to the single pressure extremum case analyzed in Umurhan (2010). For the case where $-0.5\Omega_0 < \omega_a^+ < 1.5\Omega_0$ is a maximum value of $\alpha\Delta^+ \approx 0.53$ beyond which there is no instability. As $\alpha\Delta^+ \to 0$ the critical value of ω_a^+ for instability also approaches zero which essentially means that all values of ω_a^+, positive or negative, have some potential for instability so long as the jet widths are thin enough. This latter property differs from the analogous property in the classical RWI problem wherein only anticylonic values of the deviation shear profile (i.e. $\omega_a < 0$) lead to instability. Finally, for a given value of ω_a^+ there always exists a wavenumber corresponding to the fastest growth rate indicated by a perusal of the contours shown in Figure 11.

7.3.2. Z-modes

As might be anticipated, the asymmetric jet model also supports Z-mode instability. A representative survey of the results is found in the growth rates as a function of vertical wavenumber shown in Figure 12. As in the last section, the asymmetric models are ones in which the total integrated deviation vorticity is zero, so that the flow profile is dictated only by values of $\omega_a^+, \Delta^+, \Delta^-/\Delta^+ = \delta$ with ω_a^- given by (54). We consider horizontal wavenumber values of $\alpha = 1.3$ which is approximately the smallest non-zero wavenumber appropriate for the numerical experiments of M13.

Figure 12 shows the growth rates for four different values of ω_a^+ holding Δ^+, δ and α fixed. The results show that if the jet amplitude ω_a^+ lies between 0 and ω_{ac1} with $\omega_{ac1} \approx -0.104\Omega_0$, then only a Z-mode instability is possible. This corresponds to a value of Ro slightly larger than 0.05. In this case, there is no growth for $m = 0$ and the fastest growing mode occurs for $m \approx 3.5$ - which is similar to the periodic pattern seen in the emerging crystallization profile of Figure 2d of M13. However right at $\omega_a^+ = \omega_{ac}^+$ (the dashed curve in Figure 12) the $m = 0$ state also becomes marginal. Coincidentally this critical value of ω_{ac1}^+ is approximately the same marginal condition for the RWI and this is borne out by an inspection of the marginal boundary shown in Figure 11 (see the location where the two hatched lines meet). When the magnitude of the jet's amplitude exceeds this marginal value, i.e. for $\omega_a^+ < \omega_{ac1}^+$, then the the growth curves show growth also for vertically uniform perturbations indicating the concurrence of the Z-mode instability and the RWI. The Z-mode instability is clearly evident as the maximum growth rate still sits around the $m \approx 3.5$ value, however, its presence is diminished by the growing importance of the RWI as the magnitude of ω_a^+ increases well past the corresponding magnitude of ω_{ac1}^+ (see the solid curve in that same figure).

In conclusion we find that, irrespective of the sign of ω_a^+, an asymmetric jet profile can support both the RWI and the Z-mode instability provided the jet's amplitude is sufficiently strong, in other words, jets are unstable and likely undergo nonlinear destructive transformation
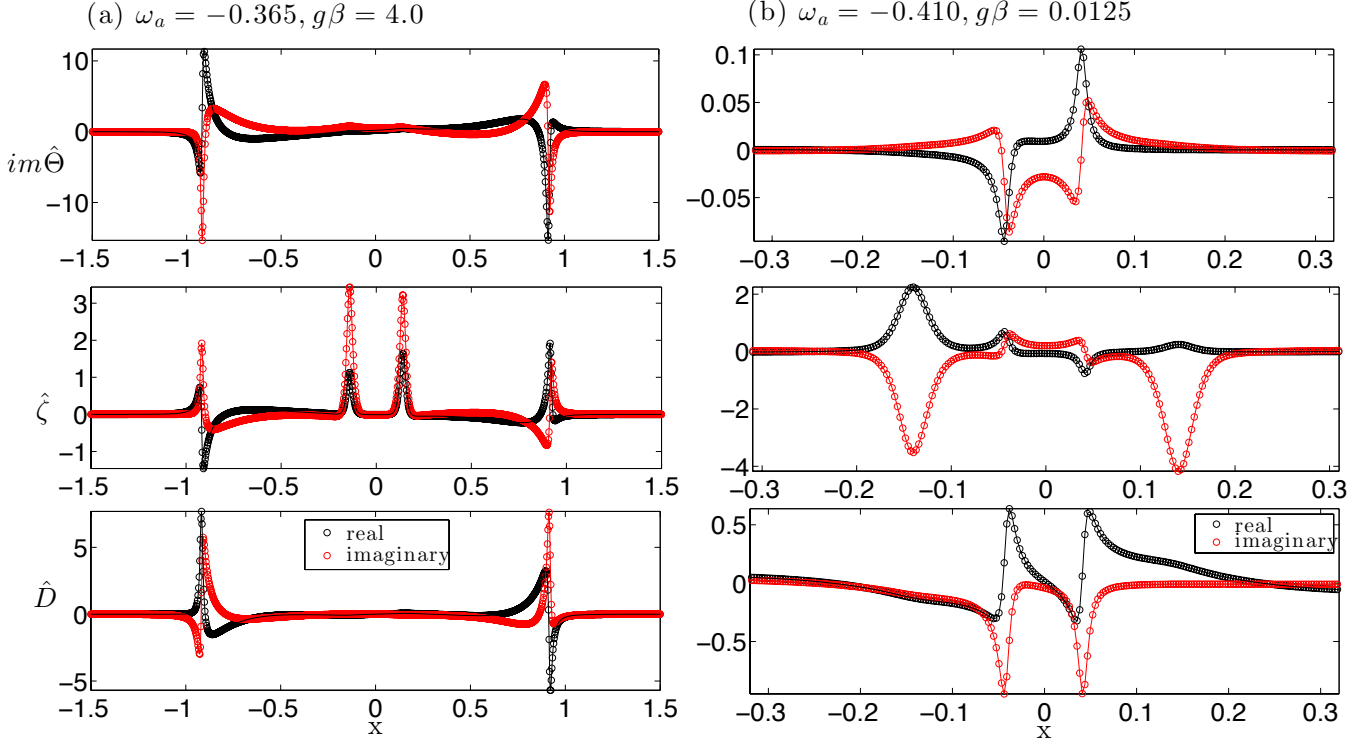
Figure 9. Perturbation eigenfunction profiles $\hat{\Theta}, \hat{\zeta}$ and $\hat{D}$ in two shear layer models. Panel (a): $\omega_a = -0.365, g\beta = 4.0, m = 5.9$ with growth rate $-\text{Im}(\omega) \approx 0.02$. Panel (b): $\omega_a = -0.410, g\beta = 0.0125, m = 2.1$ with growth rate $-\text{Im}(\omega) \approx 0.018$. In both panels $\alpha = 1.4$ and $\Delta = 0.14$ together with $\epsilon = 0.02$. The locations of these two models in parameter space are indicated by yellow squares labelled "a" and "b" in Fig. 8. The buoyant critical layers and their locations are predicted according to Eq. (37) with ω set to zero: for panel (a) $x_{bg} = \pm 0.91$ while for panel (b) $x_{bg} \approx \pm 0.042$ and these are most prominent in both the $\hat{\Theta}$ and $\hat{D}$ fields. The imprint of the edges of the jet at $x = \pm 0.14$ is apparent in the $\hat{\zeta}$ field shown in both panels. Note the critical layers appear inside the shear layer for the model shown in Panel (b). All values of ω_a and ω quoted in figures are in units of Ω_0, while units of $g\beta$ are Ω_0^2. Solutions developed on domain $|x| < \pi$ and for values of m approximately corresponding to the fastest growth rates.
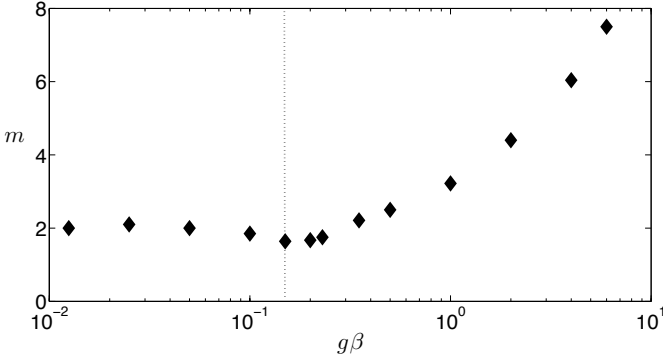

Figure 10. The values of the vertical wavenumber m corresponding to the marginal instability transition in the vicinity of $\omega_a = \omega_z$. Values are shown as a function of $g\beta$ for the values of α and Δ given in Figure 8. Values of wavenumber m in azimuthal box scale units of $L = 2\pi$. $g\beta$ in units of Ω_0^2. The vertical dotted line corresponds to the value of $g\beta = N_c^2$ (see previous figure).

if $|\omega_a^{\pm}|$ is large enough. We examine the basis for this expectation in the following section.

8. NONLINEAR MANIFESTATION: JETS BEGETTING JETS.

While this is a linear examination, it is instructive to see how this unstable mode drives nonlinear power. In particular, we assess the nonlinear terms in the vorticity equation (7) using the linear solutions we have

just determined. There are six possible nonlinear forcing terms. Because the nonlinearities are quadratic, these will project power into different wavenumber disturbances. By example, let us analyze the transport terms – familiar in atmospheric dynamics and meteorology – and focus on the radial component expression $-u\partial_x \zeta$. Given the normal mode form in which disturbances are $\sim e^{i(\alpha y + mz)}$, the above products give power in the vertically-azimuthally uniform "mean" state

$$= Re\left(\hat{u}\partial_x \hat{\zeta}^*\right),$$

where the star appearing means complex conjugate. We refer to this as the *mean-forcing.*. There is also power in the product wave numbers 2α and $2m$,

$$= \left(\hat{u}\partial_x \hat{\zeta}\right)e^{2i\omega t}e^{2i(\alpha y + mz)} + \text{c.c.}$$

and we refer to this as the *2k-forcing*. We assess these various contributions for all of the nonlinear forcing terms appearing in equation for which we call accordingly: the azimuthal component of the transport $-v\partial_y \zeta$, the vertical component of the transport $-w\partial_z \zeta$, the nonlinear vertical stretch $\zeta\partial_z w = -D\zeta$, and the vortex tilting effects $\zeta_x \partial_x w + \zeta_y \partial_y w$. In the following two sections we examine the nonlinear forcing in the vorticity-step and jet models.

8.1. *Nonlinear forcing in the vortex step model*

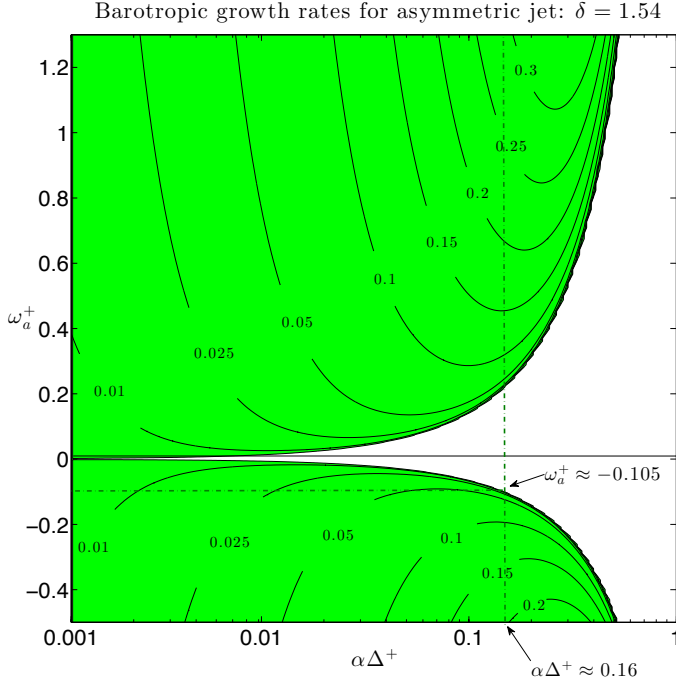Barotropic growth rates for asymmetric jet: $\delta = 1.54$

Figure 11. Contour plots of growth rates of the barotropic asymmetric jet profile on the $\alpha\Delta^+$ - ω_a^+ plane. Other properties of jet are fixed in which: $\Delta^- = \delta\Delta^+$ together with $\omega_a^- = -\omega_a^+\Delta^+/\Delta_- = -\omega_a^+/\delta$ (see text). This particular plot corresponds to $\delta \approx 1.54$. Shaded regions correspond to the RWI of this barotropic jet. Growth rates are in units of Ω_0. Vertical hatched line corresponding to $\alpha\Delta^+ \approx 0.16$ indicating the parameter values later examined in Section 7.3.2.
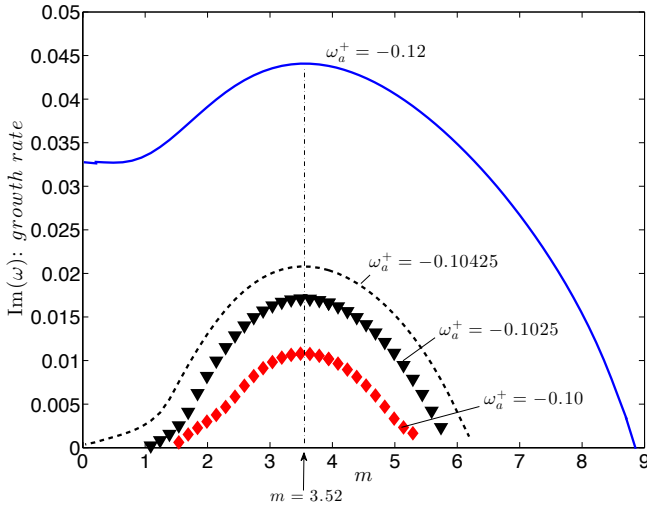

Figure 12. Growth rates (in units of Ω_0) in asymmetric jet model with $\epsilon = 0.02$, $g\beta = 4\Omega_0^2$, $\Delta^+ = 0.13$, $\Delta^- = 0.20$ (i.e. $\delta \approx 1.54$), and $\alpha = 1.3$ for four different values of ω_a^+ with ω_a^- fixed and equal to $-\omega_a^+\Delta^+/\Delta^-$ (values of ω_a^+ in units of Ω_0). The dashed curve signifies the critical value of ω_a^+ in which the RWI begins to also get expressed (and corresponds to the critical criterion indicated by where the two hatched lines meet in Figure 11). In all curves shown, the fastest growth rate corresponds to $m \approx 3.5$.

Figure 13 exhibits each of the six individual forcing profiles as well as the aggregate resulting forcing in the vorticity step model examined in Section 7.1. As expected, there is strong power in both the mean-forcing and the first harmonic (hereafter called *2k-forcing*) at $x = 0$ and it is dominated by the radial transport term $u\partial_x\zeta$. This is understood to represent the primary vortex step either rolling-up or undergoing a large amplitude undulation (e.g., Tamarin et al. 2015). There is strong amplitude power in both the mean-forcing and 2k-forcing at the critical point $x_{bg}^+ \approx 0.62$. The vorticity forcing there is that of a jet (for comparison see the vorticity profile associated with the barotropic jet in Figure 1b), which means that as the Z-mode instability develops, there will nonlinearly emerge a jet like structure in the critical layer.

What is unexpected is that the amplitude of this vorticity forcing at x_{bg}^+ is driven primarily by the vortex tilting terms: perturbations in the velocity fields give rise to perturbations in the horizontal vorticity components ζ_x', ζ_y'. These, in turn, nonlinearly couple to the perturbation vertical velocity w' – in the critical layer these nonlinear products act as source terms generating vertical vorticity. The radial transport term also contributes significantly in the critical layer, but generally acts opposite to the vorticity generation driven by the vertical tilting of horizontal vorticity. In all instances we have calculated, the aggregate vortex forcing is non-zero and always dominated by the vortex tilting terms, and mainly by the vertical tilting of the radial vorticity $\zeta_x\partial_x w$. We also note that the vortical forcing at x_{bg}^- is comparatively weak although non-zero. It is remarkable that there is strong power in both the mean and 2k forcings indicating that this instability is quite powerful where it is expressed since many vertical wave numbers are excited (see the discussion on growth rates and their dependence on the vertical wave number m, found in the previous sections). Its expression, however, is constrained to within a narrow zone of the critical layer whose width depends upon the growth rate itself: faster growth rates mean wider the critical layer zones (see further below).

8.2. *Nonlinear forcing in the jet model*

The nonlinear expression of the instability in the jet model field (Sections 7.3.1–7.3.2) also underscores the implications we have inferred in the previous section. For conditions in which $\omega_{ac1}^+ < \omega_a^+ < 0$ the nonlinear forcing is strongest at the model jet's associated critical layers while it is relatively weak at the location of the jet itself as indicated in both Figures 14–15. These figures also emphasize how strongly localized the vortical forcing is to the buoyant critical layer zones. As in the vortex step case examined in Section 6.1, these figures also clearly exhibit how (i) the emergent vertical vorticity profile is yet another jet and (ii) the two *main* competitors in the nonlinear vertical vorticity driving is between the vertical tilting of the radial perturbation vorticity and radial advection of the perturbation vertical vorticity with the former outlasting the latter.

However, when the the magnitude of the model jet increases so that we are now in a parameter regime with $\omega_a^+ \leq \omega_{ac1}^+$, then the character begins to change. Near the
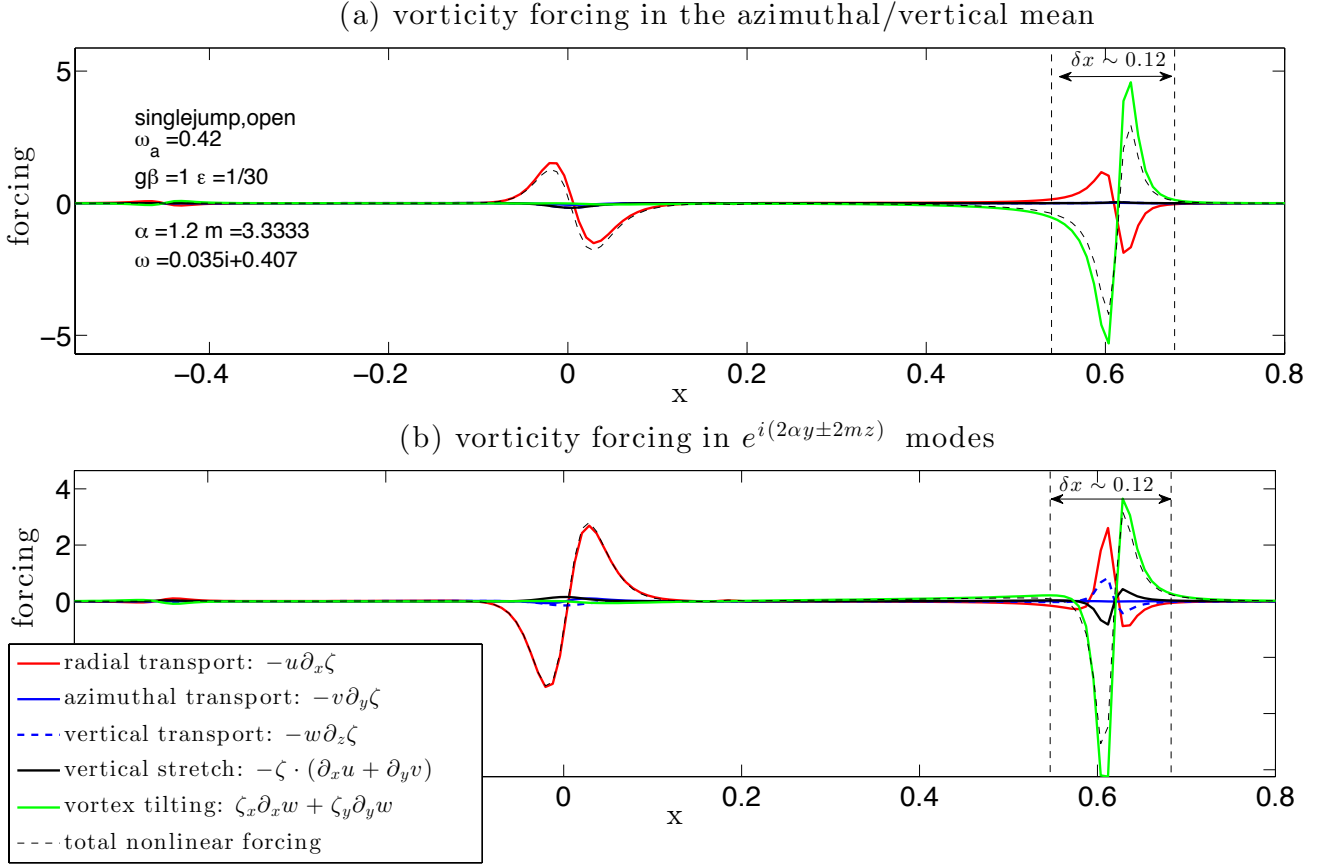
(a) vorticity forcing in the azimuthal/vertical mean

(b) vorticity forcing in $e^{i(2\alpha y \pm 2mz)}$ modes

Figure 13. Nonlinear vorticity forcing based on the solutions shown in Figure 3. As detailed in the text (Section 4), individual and aggregate vorticity forcing shown for (a) mean-forcing and, (b)2k-forcing. The dashed black line shows the aggregate of the six individual forcing terms shown in the boxed legend of panel (b). The radial transport forcing is strongest at $x = 0$, where the location of the mean vorticity gradient is greatest, but it also has a significant contribution at the critical layer $x^+_{bg} \approx 0.62$. However, the vortex tilting terms (green) outcompete the radial transport contribution at $x = x^+_{bg}$. The mean-forcing profile indicates that a jet-like feature should develop at $x = x^+_{bg}$, while the strong 2k radial transport forcing at $x = 0$ suggests that the vortex profile there should eventually get destroyed. Denoted on the figure is the width of the critical layer δx, as determined in the linear analysis section. For parameters shown on this figure and subsequent ones, rates are in units of Ω_0, $g\beta$ in units of Ω_0^2 while lengths and wavenumbers in L and L^{-1} respectively.

marginal condition for the onset of the RWI ($\omega_a^+ \approx \omega_{ac1}^+$) Figure 16 shows how nonlinear vertical vorticity forcing at the location of the jet is slightly larger in magnitude than the corresponding forcing at the buoyant critical layer zones. We also note that the nonlinear vortical forcing upon the model jet is mainly in the region $0 < x < 0.2$. Given the value of $\omega_a^+ \approx -0.12\Omega_0$ it means that *the nonlinear driving is focused mainly on the anticyclonic side of the asymmetric jet* suggesting that this will ultimately result in the nonlinear roll-up of that part of the jet - something that is seen throughout the numerical experiment reported in M13. Eventually, when the value of ω_a^+ is strongly in the RWI instability regime (i.e. $\omega_a^+ < \omega_{ac1}^+$) the nonlinear forcing is almost entirely focused upon the anti-cyclonic side of the model jet with relatively little corresponding forcing power at the critical layer zones or the cyclonic side of the jet (Figure 17).

Although not shown here, the same qualitative pattern holds if ω_a^+ is sufficiently positive. For example we have examined the results using the same model jet dimensions assumed for the results shown in Figures 14–

17 including the value of $\alpha\Delta^+ \approx 0.16$, $\delta \approx 1.54$ and $g\beta = 4\Omega_0^2$ where, instead, we examine the response for positive values of ω_a^+. Inspection of Figure 11 shows that the corresponding value of the onset of the RWI for the jet is given by $\omega_{ac2}^+ \approx 0.22\Omega_0$. The same pattern of results follows - for $0 < \omega_a^+ < \omega_{ac2}^+$ only the Z-mode instability is expressed and the nonlinear vortical forcing is dominant in the critical layer zones. Similarly, as $\omega_a^+ > \omega_{ac2}^+$ the RWI becomes more important in which the nonlinear vortical forcing is dominant in the vicinity of the model jet. In particular, the forcing is concentrated in the region $-0.2 < x < 0$ but this also happens to be the anti-cyclonic side of the model jet since $\omega_a^+ > 0$ means $\omega_a^- < 0$ according to equation (54).

8.3. *Jets begetting jets?*

M13 consider the fluid response of a stably stratified Keplerian shearing box to an azimuthally aligned tube of surplus vertical vorticity placed in the origin of their experiment. They find that after some time, the fluid domain steadily transitions into similarly confined narrow/tubular regions of deviation jet-like profiles. For a
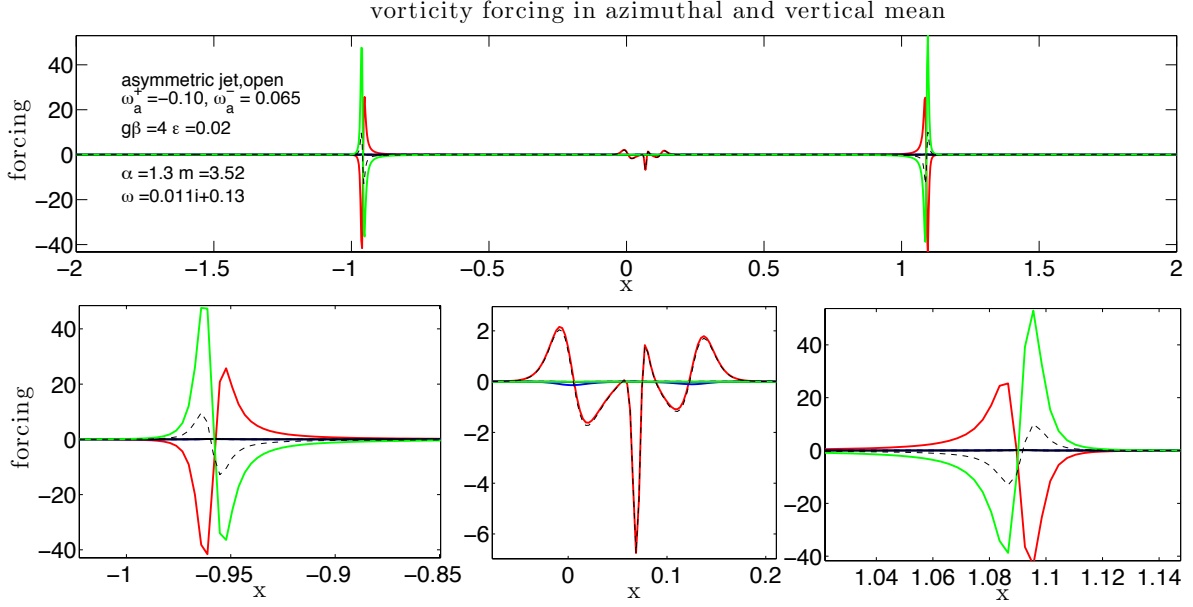
vorticity forcing in azimuthal and vertical mean

Figure 14.   Nonlinear vorticity forcing in the mean for the asymmetric jet profile with $\alpha = 1.3$ $\Delta^+ = 0.13$, $\Delta^- = 0.20$ and $\omega_a^+ = -0.1$ (with $\omega_a^- = 0.065$) and $g\beta = 4$, the latter being comparable to conditions examined in M13. The model flow profile has an effective Ro ~ 0.05 The vertical wavenumber $m = 3.52$ corresponding to the fastest growth rate ($\text{Im}(\omega) \approx 0.011$) of the dispersion curve associated with the diamonds shown in Figure 12. Top panel shows the distributed forcing power over space and the lower row of panels shows closeups of the active regions. Note the relative weakness of the nonlinear power near the location of the forcing jet for this relatively weak value of ω_a^+. The instability for this parameter regime is dominated by the Z-mode instability and the the nonlinear power is concentrated mostly in the critical layer zones ($x_{bg}^- \approx -0.96$ and $x_{bg}^+ \approx 1.09$) where vortex tilting and radial transport are the dominant forms of vortex forcing. 1750 grid points were used in generating these solutions. All quoted quantities scaled according to convention described in Figure 13.
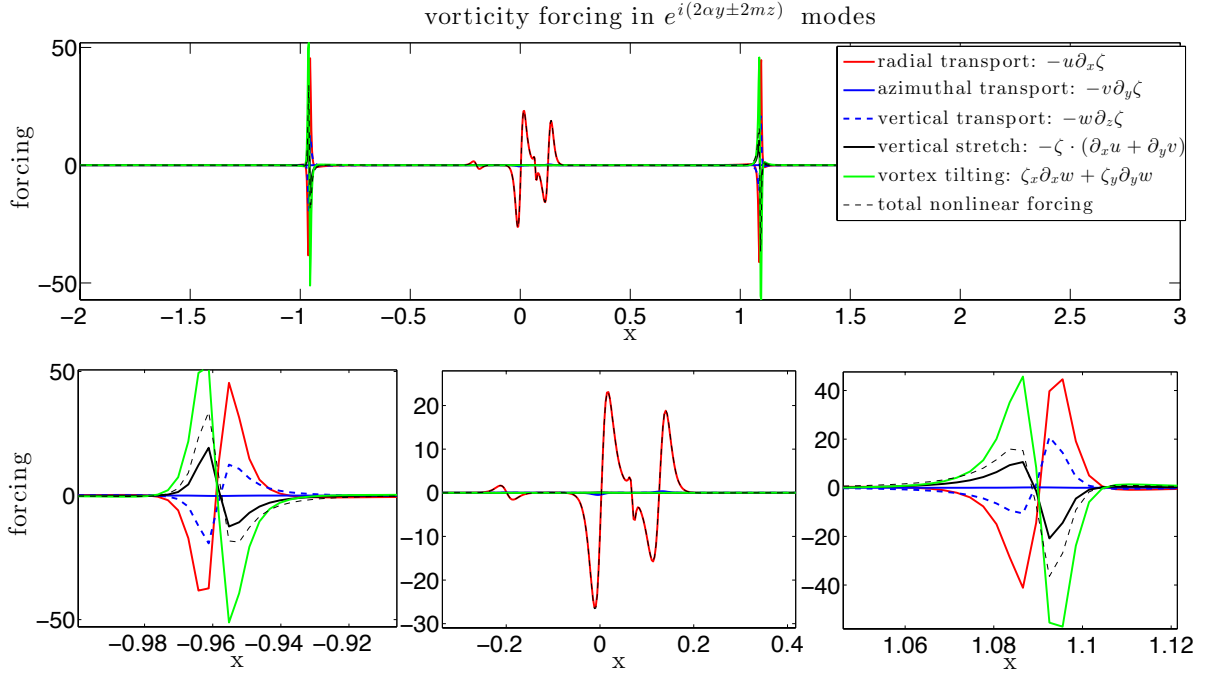
vorticity forcing in $e^{i(2\alpha y \pm 2mz)}$ modes

Figure 15.   Like Figure 14 except the forcing power in the 2k modes shown.

(a) vorticity forcing in azimuthal and vertical mean

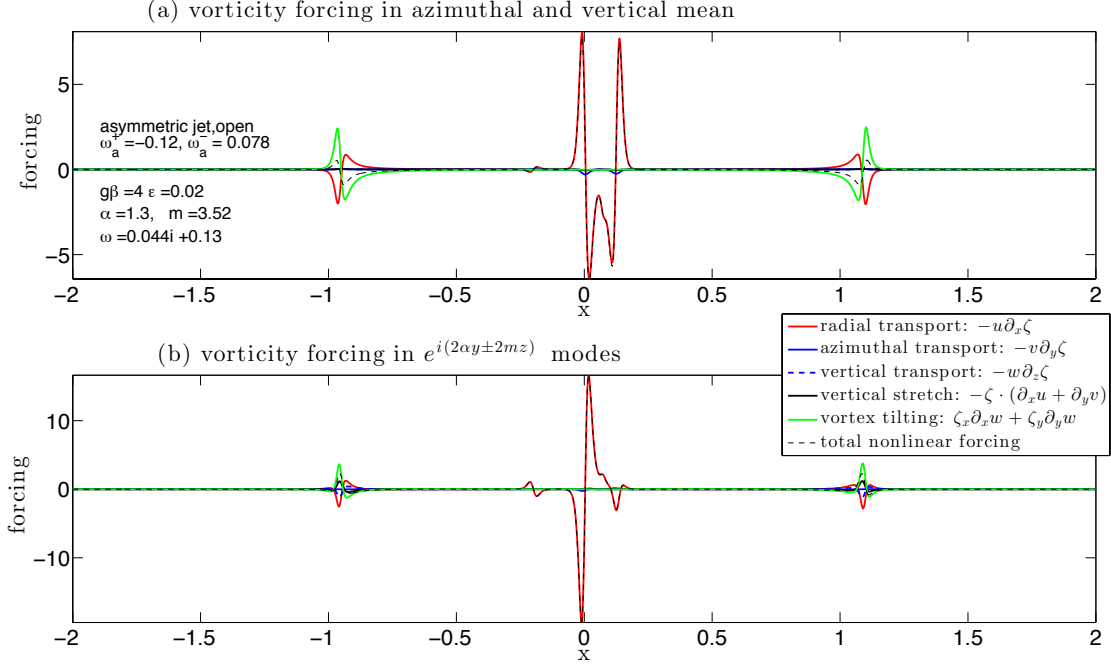(b) vorticity forcing in $e^{i(2\alpha y \pm 2mz)}$ modes

Figure 16. Like Figure 14 except $\omega_a^+ = -0.12$ (and $\omega_a^- = 0.078$), which means this is a model flow profile with Ro ~ 0.06: (a) top panel forcing in the mean and (b) forcing in 2k. The nonlinear properties depicted are those for the fastest growing mode shown in Figure 12 (solid line). The system supports both Rossby and Z-mode instabilities in which the former is more strongly expressed than the latter. The nonlinear forcing, mostly due to the radial advection of the mean vorticity gradient, is strongest now near the location of the original jet itself and is relatively weak at the buoyant critical layers (near $x = -1$ and $x = 1.1$). This strong power, especially in the 2k forcing, is indicative of nonlinear roll-up of shear layers. Scrutiny of the forcing shows that it is focused in the region $0 < x < 0.2$ which, given that $\omega_a^+ < 0$, corresponds to the anticylonic side of the model jet profile. All quoted quantities scaled according to convention described in Figure 13.
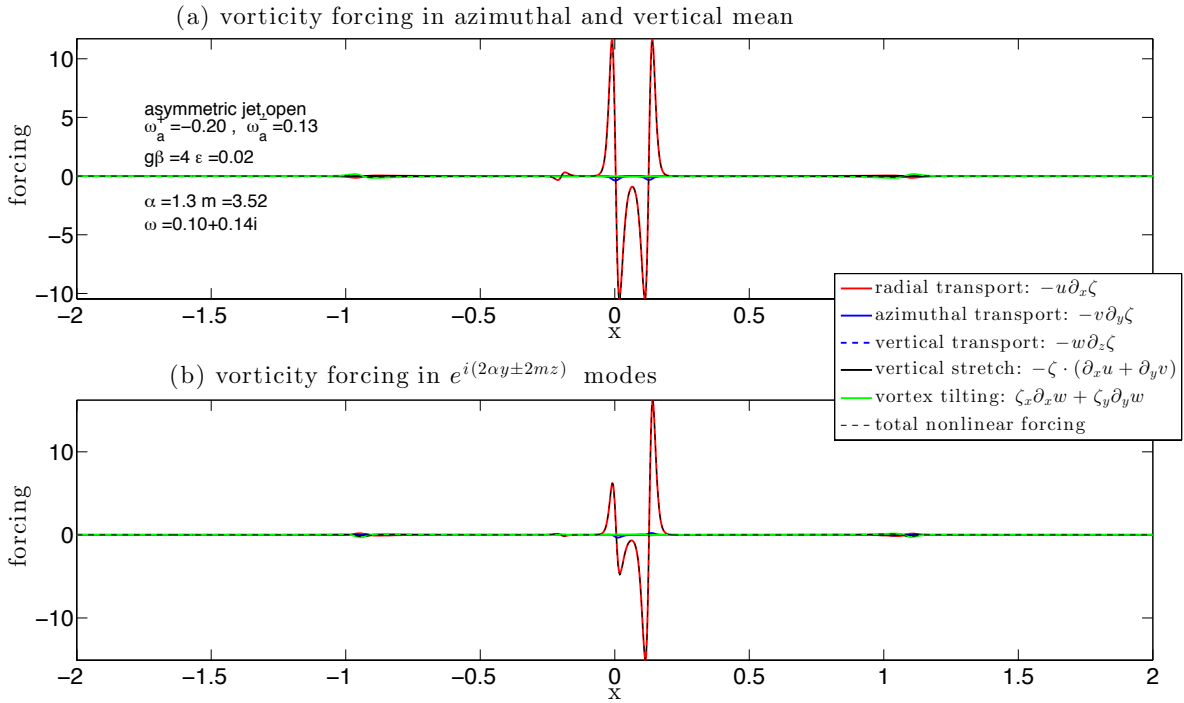
(a) vorticity forcing in azimuthal and vertical mean

(b) vorticity forcing in $e^{i(2\alpha y \pm 2mz)}$ modes

Figure 17. Like Figure 14 except $\omega_a^+ = -0.2$ (and $\omega_a^- = 0.13$), which that this is a model flow profile Ro ~ 0.1: (a) top panel forcing in the mean and (b) forcing in 2k. The instability, Im(ω) ≈ 0.1, is almost totally dominated by the Rossby wave instability with very weak power at the location of the buoyant critical layers. Similar to the previous figure, most of the nonlinear forcing is concentrated on the anticyclonic side of the model jet profile. All quoted quantities scaled according to convention described in Figure 13.

surplus vorticity field placed at the origin containing the midplane, the response flow generates jet like vertical vorticity above and below the mid plane at the location of buoyant critical points. A close inspection of both Figures 1 and 2 of that work shows that the generated jet-like vertical vorticity fields (the original children) have some vertical extent. As the simulation marches forward in time, these original child vortices themselves become parents to a new generation of child vortices at new critical layers associated with their parents, and so on the process continues.[12] The results and intuition derived from the linear study considered here largely confirms this self-replicating scenario proposed in M13.

The insights garnered of the analysis here helps to fill in more of the details of this emergent (possibly) turbulent self-sustaining process. A vorticity field supporting a localized Rossby wave will generate a new vorticity field at a far-field buoyant critical layer. This buoyant critical layer x_{bg} is found to be the location where the Doppler shifted frequency of the Rossby wave is resonant with the local Brunt-Väisälä frequency. The resonance induces a vortex generation mechanism which is dominated by two mostly opposing processes: (i) the local creation of vertical vorticity in which the local perturbation radial vorticity (i.e. the ζ_x found in the region around $x = x_{bg}$) is converted into vertical vorticity through the vertical tilting process: $\zeta_x \partial_x w$, and (ii) the local (again near $x = x_{bg}$) radial advection of the perturbation vertical vorticity: $u' \partial_x \zeta$. Both effects act nearly opposite to one another, but the vertical tilting mechanism appears to dominate in the jet profiles we have tested here in this study.

Among other things, this results in an asymmetric jet-like structure which grows in amplitude until it either saturates or the jet itself gets destroyed because of roll-up due to the RWI. While the spawned jet grows it can, on its own accord, induce new jet-like structures at new critical points associated with the spawned jet and the linear analysis done here largely supports the picture sketched in M13 of *jets begetting jets*. As a "parent" structure, a jet-like profile can give rise to new "child" jets only while the parent jet maintains its structural integrity. This can be inferred from the linear stability of the asymmetric jet examined in Section 6.3: as the amplitude of the jet $|\omega_a^\pm|$ is increased from zero first only Z-modes are unstable. However, as $|\omega_a^\pm|$ increases eventually the most unstable mode is the RWI which induces transformative/destructive roll up of the parent jet. It is only during the low amplitude range of jet amplitudes, prior to the RWI becoming important, will a given jet generate into existence a new jet(s) at its associated buoyant critical layer(s).

In this way, the parent jet must stay as such long enough for child jets to grow into maturity so they too can generate the next generation of jets, and so on perpetuating the self-replication process. Critical to this

is the time spent growing each jet - as it must grow slow enough so that the Z-mode instability (which is relatively slow by our current account) may manifest itself and start spawning the next generation of jets. If a jet grows too fast then the Z-mode process has no time to birth the new generation and the whole process shuts off. If the jet grows quite slowly it could, in a general sense, give rise to a pattern state like that reported in M13. Conditions lying somewhere between these two extremes might give rise to a turbulent flow state that could be either decaying or self-sustaining - perhaps something in the flavor of a "chaotic propeller" identified as being operative in subcritical transitions in both plane-Couette and rotating-plane-Couette flows (e.g., see discussion in Rincon et al. 2007).

Whether or not this process can be self-sustaining and lead to a turbulent state under a wide umbrella of conditions appropriate to Dead Zones remains to be determined. It would seem, however given our considerations, that its self-sustainability depends centrally on what way the original disturbances are structured since it requires there to be some relatively large amplitude disturbance to start the whole thing off. A recent announcement by Marcus et al. (2015) on this process in a shearing sheet disk model with vertically varying gravity and stratification seems to indicate that it can give rise to a strongly turbulent state.

8.4. *Spatially localized instability*

In Section 7.2 we examined the properties of the shear layer system and we identified that there is a critical value of the Brunt-Väisälä frequency N_{cr} for which the location of the critical layer goes from being found outside the shear layer ($g\beta > N_{cr}$) to appearing inside the shear layer ($0 < g\beta < N_{cr}$). The discussion in the previous section concerning the self-reproductive spatial spreading of jet creation/destruction is the expected outcome of the former of the two conditions. What might happen when the critical layer appears inside the shear layer?

Consider the nonlinear vorticity forcing arising from the conditions shown in Figure 9b in which the critical layer is clearly inside the shear layer and the shear layer itself is stable against the destructive RWI. We show in Figure 19 the corresponding mean vertical vorticity forcing profile arising under these parameter conditions $g\beta < N_{cr}^2$. The imprint of the primary shear layer is evident in the vicinity of the locations $x \approx \pm 0.14$ while the nonlinear forcing at the critical layer is also clearly visible near $x \approx \pm 0.045$. The resulting aggregate forcing profile qualitatively resembles forcing profiles we have discussed thus far for when the critical layers appear outside. We observe that unlike the examples of the vorticity-step and jet profiles, the critical layer jets are primarily driven by the radial advection of the perturbation vertical vorticity ($-u \partial_x \zeta$) while the vertical tilting of radial perturbation vorticity ($\zeta_x \partial_x w$) is relatively weak by comparison but acts with the same sense as the radial advection of the perturbation vertical vorticity.

The implications are interesting: These results suggest that under those conditions in which the Brunt-Väisälä frequency is small, that jets will grow inside the shear layer and, as per our earlier insights, once the jet amplitude grows large enough it will self-destruct while gen-
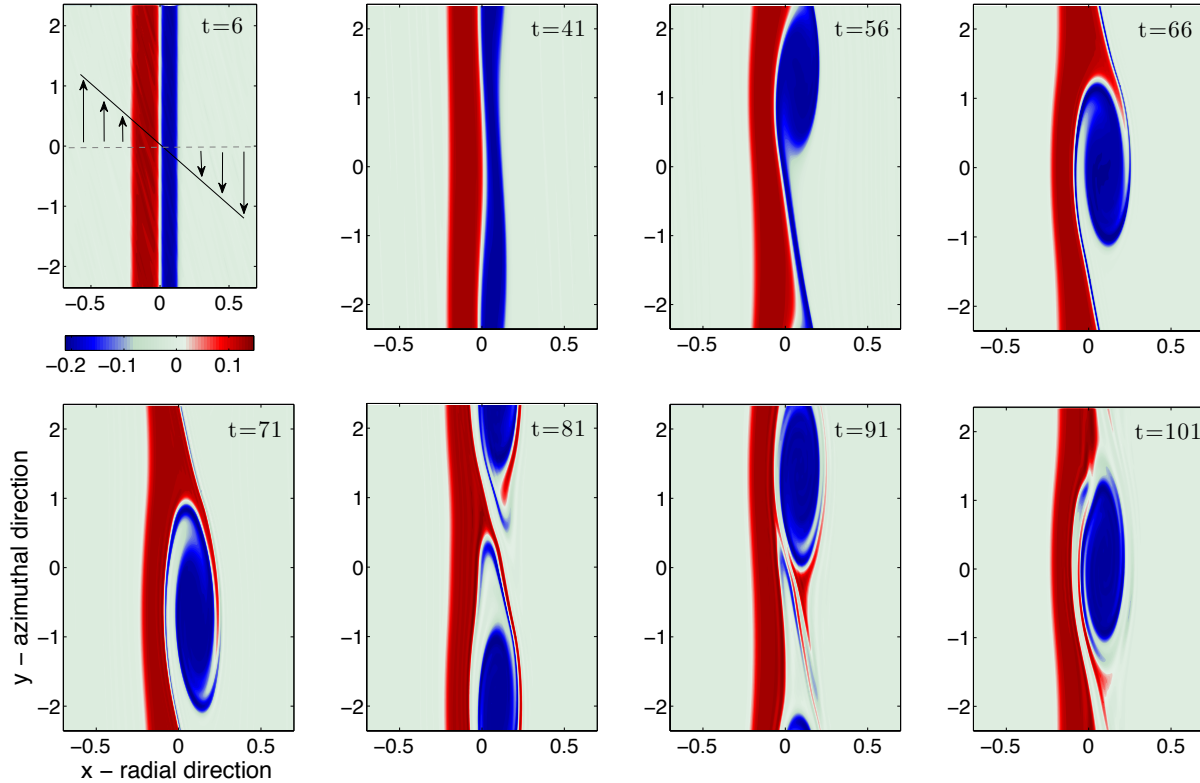
---

[12] We observe that in the numerical experiment results presented in M13, the original tube of surplus vertical vorticity located at the origin remains constituted as such throughout the duration of the domain and does not get destroyed. This is probably because the the width and girth of this line charge vorticity is one which does not go unstable via the RWI (or its equivalent analog for such a model flow). Further analysis needs to be done to confirm this conjecture.

Figure 18. Two dimensional simulation of the RWI roll-up of the asymmetric jet problem examined in Section 7.3.1 with $\omega_a^+ = -0.2\Omega_0$, $\omega_a^- = -0.13\Omega_0$ with $\Delta^+ = 0.13$ and $\Delta^- = 0.2$ and $\epsilon = 1/50$. Numerical experiment done on a domain $|y| \leq 3\pi/4$ and $|x| \leq \pi/2$, however only the range $|x| \leq 0.70$ shown. Deviation vertical vorticity profiles shown where the corresponding Rossby numbers are given by Ro $= |\omega_a^\pm|/2\Omega_0$ which here means that the peak activity is in the range of 0.05 to 0.1. The eight panels shown are the sequential development in time (in units of Ω_0^{-1}, where $t = 2\pi$ means one local disk orbit time). The first panel shows the sense of the prevailing Keplerian shear. Roll up is focused only on the anticyclonic part of the jet profile (the parts shaded in blue) while the cyclonic portion retains its original integrity, if however, some vortex filaments are created from it during the latter stages of roll-up of the anti-cyclonic side. Simulations done using the spectral method outlined in Tamarin et al. (2015) using a radial and azimuthal grid of $N_x = 512$ and $N_y = 192$ points respectively. (high radial resolution was used in order to resolve the transition region of the original model jet since $\epsilon = 0.02$.) A 3/2 dealiasing rule is used, as well, a Shapiro filter is applied to filter out 2h-grid scale waves. No other additive artificial viscosities applied. Note that the radial scale shown in the figures is exaggerated compared to the horizontal scale.

erating new jets associated with its critical layers. If the whole process remains confined to inside the shear layer, then there are at least two possible outcomes: In the first of these, the parent shear layer structure remains stable (also as suggested by linear analysis) while the jet inside grows and once having reached a sufficient amplitude it will self-destruct having spawned child jets along the way (presumably contained inside the shear layer as well). The second possibility is that while the jet inside grows, the parent shear layer nonlinearly destructs as well. If an external agent is responsible for the creation and maintenance of the parent shear layer in the first place – e.g, by either direct thermally driven relaxation (Les & Lin, 2015, Lobo Gomes et al., 2015) or by the VSI (Richard et al., 2015) – then either of the two scenarios envisioned could give rise to a process of unsteady jet creation and destruction entirely contained inside the shear layer, where the only difference in the outcomes of the two possibilities is the degree of the unsteady activity – possibly turbulent. Global numerical calculations of the several processes mentioned (thermally driven relaxation or the VSI), when sufficiently resolved, can test whether or not this dynamical scenario indeed manifests itself.

9. SUMMARY DISCUSSION

This study independently confirms and complements the Z-mode process and effect uncovered and reported in M13. We assert that the Z-mode instability is a bonafide instability of a sheared system not supporting the more familiar centrifugal instability studied in the context of the Taylor-Couette system.

We have adopted an alternative mathematical framework to analyze the linearized problem of perturbations in a strongly sheared and stratified atmosphere. The relatively sophisticated approach, which involves converting the underlying linearized differential system instead into a set of coupled integral equations, is here undertaken because of the complexities inherent to discerning eigenmode structure of PDEs supporting one or more irregular singular points. In this problem, those singular points are the buoyant critical layers responsible for the instability.

The single-step vorticity jump examined at length in Section 7.1 exhibits the Z-mode instability stripped down to its bare minimum ingredients, that is, a stably stratified atmosphere with a shear profile $v_0(x)$ containing (at least) one location with a strong radial gradient which, in turn, supports a radially localized Rossby wave which
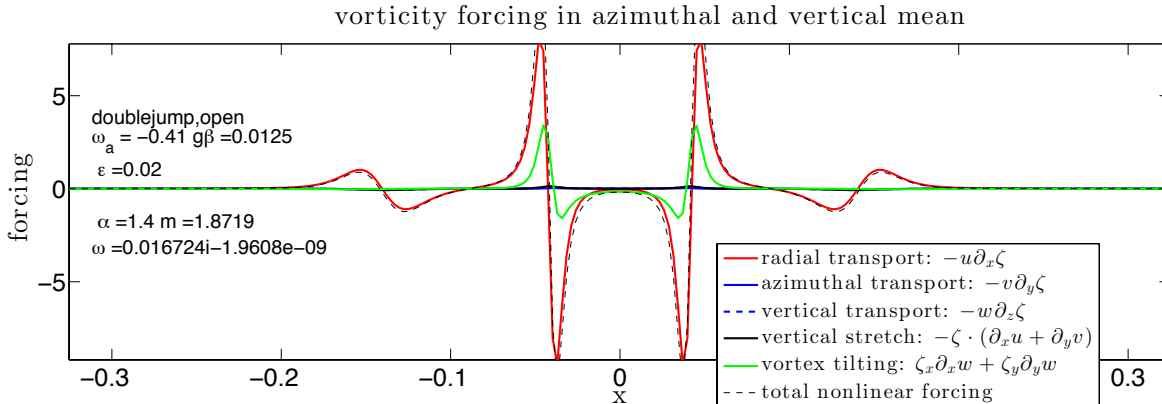
vorticity forcing in azimuthal and vertical mean

Figure 19. The nonlinear vorticity driving for the linear solutions shown in Figure 9b. In this example the critical layer exists inside the shear layer near $x = \pm0.45$. The edges of the jet are at $x = \pm0.14$. All shears and growth rates in units of Ω_0 while $g\beta$ in units of Ω_0^2.

is the basic carrier mode of the Z-mode instability. Supposing this Rossby wave is vertically uniform and has a wavelength $\lambda_\alpha = 2\pi/\alpha$ with corresponding propagation speed c_{rw}, on its own accord it will not become unstable. However, because the atmosphere is stratified with a squared Brunt-Väisälä frequency $N_B^2 \equiv g\beta$, sufficiently far from the center of the Rossby wave there exist radial locations $x_{bg}^\pm$ in which the location specific value of the background shear flow plus the local *vertically uniform* inertia-gravity wave propagation speed $\pm N_B/\alpha$ is equal to the Rossby propagation wave speed,

$$c_{rw} = v_0\left(x_{bg}^\pm\right) \pm \frac{N_B}{\alpha}, \tag{56}$$

that is to say, the location of the buoyant critical layer. Said in another way, *there is a frequency resonance* in which the locally observed Doppler shifted Rossby wave frequency equals the absolute value of the local Brunt-Väisälä frequency. This result directly confirms the stated requirements for instability as reported in M13.

The growth rates of Z-modes are shown in all three flow models to be maximal at some non-zero vertical wavenumber which depends upon the amplitude and type of model shear flow under consideration. Although the shear layer model considered here and the setup considered by M13 are formally different, we consider them to be similar enough to compare our results with theirs. Using parameter values that are qualitatively most similar to their setup, we confirm that the Z-mode instability gets expressed around values of Ro ≈ 0.20.

The jet flow models we have considered show that the unstable Z-modes exist for values of Ro ≈ 0.05 thereby pushing down the critical values of Ro needed to express the instability by a factor of four of that surmised in M13. These trends and results emphasises the need for a general assessment the Z-mode instability including necessary conditions.

The vertical velocity fluctuations are highly localized in narrow regions containing the critical layer as, e.g., Figure 4(c) plainly depicts. The localization scales linearly with the growth rate of the Z-mode - a lower growth rates means a narrower critical layer zone. This trend is probably why many previous numerical simulations (prior to M13), conducted both in shearing sheet and cylindrical

geometries, have been unable to see any evidence of this effect.

We have examined with some detail the conditions in which unstable Z-modes exist both independently of and concurrently with the RWI in the shear-layer model. Using conditions similar to that examined in M13 (namely, fixed horizontal box size and shear layer width) we demonstrate for shear layers whose amplitudes ω_a lie between $\omega_Z > \omega_a > \omega_R$ that Z-modes exist in the absence of the RWI. The condition $\omega_a = \omega_R$ is the condition for the onset of the RWI and for values of $\omega_a < \omega_R$ both instabilities are present. ω_Z, which is the critical value of the onset of Z-modes, is a function of the Brunt-Väisälä frequency $g\beta$ and the former's dependence upon the latter was numerically determined for the special case considered and summarized in Figure 8. It is unexpected that the instability persists even in the limit where the stratification vanishes $(g\beta \to 0)$ suggesting that plain inertial modes in the shearing sheet should also be unstable under suitable conditions in the presence of any number of model flows like those considered here. This remains to be further examined.

The qualitative trends regarding the existence of Z-modes and their concurrence with the RWI reported above for the shear layer carry over to the jet flow model as well. However, the same relatively detailed analysis done for the shear layer model remains to be done for the jet flow model.

Given the calculated perturbation responses including the derived velocity and vorticity fields, one can assess the total nonlinear vertical vortex forcing arising from these modes according to equation (8). What is remarkable is that at the buoyant critical layer x_{bg} there are two main competitive effects driving the nonlinear response, namely, that of the radial transport of the perturbation vertical vorticity, $u'\partial_x\zeta'$, and the vertical tilting of the perturbation radial vorticity, $\zeta_x'\partial_x w'$. Figure 13, which serves as a representative depiction of these varied forcings, shows the vertical tilting of the radial perturbation vorticity generally winning out over the radial advection of perturbation vertical vorticity and, ultimately, giving rise to a vertically/azimuthally uniform jet flow as well as power in higher harmonics in the azimuthal and vertical directions. The emerging jet flow is strongly localized

due to the size of the original critical layer. This resultant nonlinear forcing at the buoyant critical layers is the same for all three model flows examined here.

We note that the only qualitative difference in the outcome of the instability in the critical layer is in the sign in the change of vorticity across the central ridge line of the emerging jet, which depends upon whether or not $u'\partial_x\zeta'$ dominates $\zeta'_x\partial_x w'$ inside the critical layer during the growth of the instability. This is because these two forcing terms appear to act opposite to one another - at least this is so in all of the profiles we have examined while preparing this study.

We have also shown here that both jets and shear layers are subject to the RWI if their vorticity amplitudes get large enough. We have considered this in detail for the jet model flow where we find that as the amplitude of the jet approaches the critical value needed for the onset of the RWI, the nonlinear forcing upon itself increases as well (sequenced in Figures 14–17). Moreover, this nonlinear self interaction, which is separate from the nonlinear forcing occurring at the buoyant critical layers, is focused mainly on the anti-cyclonic side [13] of the jet which should cause it to undergo a roll-up type of instability.

Indeed, the study of Tamarin et al. (2015) explicitly examines how the $2k$-forcing[14] of an unstable Rayleigh shear layer is most responsible for the destructive transformation of the shear layer in the nonlinear regime. Figure 18 depicts this for a model two-dimensional simulation of an unstable jet of the kind examined in Section 7.3.1 (numerical method details discussed in figure caption) showing the nonlinear roll-up of a jet profile subject to the RWI. Only the anticyclonic part rolls up while the cylonic portion remains more or less intact. The qualitative features of the roll-up sequence of the model asymmetric jet shown mirrors that of the simulations snapshots shown in M13. We emphasize that the numerical experiment of the model jet shown in Figure 18 is two-dimensional and cannot represent the later generation of new jets at the model jet's associated buoyant critical layers. Nonetheless, the point we wish to make is the claim that this part of the process discussed in M13 can be understood independently within the framework of the RWI. A similar role of the RWI has been recently uncovered in the nonlinear development of the VSI (Richard et al., 2015).

The totality of the aforementioned results leads one into considering the possibility, as originally suggested in M13, that under suitable conditions the nonlinear outcome of this instability is that of a self-replicating dynamical mechanism of jet creation and destruction. If the circumstances are just right, this could result in widespread turbulence which could perhaps be sustained. A given parent jet flow can bring into being, through the Z-mode instability, a first generation of child jets at the buoyant critical layers of the parent. Once the amplitude of the child jets grows large enough they, in turn, bring into existence a second generation of child jets at the buoyant critical layers associated with the first generation, and

so on the process continues. However, once the vorticity amplitudes of the first generation get large enough, the jets will experience the RWI destroying the anticyclonic side of their flow profiles and, possibly, severely disrupting the orderly flow of their cyclonic sides as well. A once quiet laminar disk can undergo a transformation into a non-steady dynamical state as the creation/destruction process described herein replicates itself and spreads over the entirety of the domain.

Of course, the robustness of the overall scenario described and its relevance to real protoplanetary disk Dead Zones remains to be assessed and should be the focus of future study. Such an evaluation should center on the fact that the zombie vortex instability requires the presence of a large amplitude initial disturbance (like the three model flows considered in this study) to set off the process in the first place. How does such a configuration come about in the first place would have to be plausibly explained and somehow justified. The recent numerical work of Marcus et al. (2015), which examines this process for a more realistic disk model in which, effectively speaking with respect to our analysis, the Brunt-Väisälä frequency is a function of the vertical coordinate, reports a similar pattern of eruption of the laminar state and subsequent transformation into an unsteady dynamical flow. A parallel linear analysis like that done here but applied in the more physically relevant setting considered by Marcus et al. (2015) – in which the vertical gravity and stratification is coordinate dependent – is both challenging and awaits to be done.

It appears that our conceptions regarding the nature and development of disk activity – possibly even turbulent – have returned to some ideas that were discussed nearly 25 years ago. In an often overlooked study by Dubrulle & Knobloch (1992) the authors performed a careful analysis of a non-stratified shearing box and showed that all small amplitude disturbances are stable. They went on to argue that a pure Keplerian flow is not enough to generate an instability and they went further to stress that some other additional *finite* amplitude profile – which possesses at least one inflection point – would be necessary to instigate some kind of turbulent transition in a (non-magnetized) disk. Two previous studies done right prior to that work, namely by Lerner & Knobloch (1988) and Dubrulle & Zahn (1991), explicitly demonstrated that instability was feasible in a plane-Couette setting with a flow profile similar to the shear layer profile examined in this work. Indeed, one can argue that the RWI is an example of such an inflection point instability since the shearing box is the rotating version of classical plane-Couette flow and the flow profiles examined in the original study of Lovelace et al. (1999) contain at least one inflection point. We see the Zombie vortex discovery by M13 and Marcus et al. (2015) – as well as the linear analysis we have conducted here – as taking the vision expounded by Dubrulle & Knobloch (1992) one step further for a stratified shearing box: that a finite amplitude profile without an inflection point can lead to a critical layer instability. When this recipe is further expanded to include profiles that also have inflection points, the result can turn into a self-replicating process and if the conditions are right, the shearing box flow might very well transition into a

---

[13] Recall that parts of the shear flow are termed anti-cyclonic with respect to the background Keplerian shear flow. See discussion formal definition of this found in Section 4.

[14] as defined in Section 8.

turbulent state.

REFERENCES

Baines, P. G., & Mitsudera, H. 1994, Journal of Fluid Mechanics, 276, 327
Balmforth, N. J., & Piccolo, C. 2001, Journal of Fluid Mechanics, 449, 85
Barker, A. J., & Latter, H. N. 2015, MNRAS, 450, 21
Drazin, P. G. 2002, Introduction to Hydrodynamic Stability, by P. G. Drazin, pp. 276. ISBN 0521804272. Cambridge, UK: Cambridge University Press, September 2002., 276
Drazin, P. G., & Reid, W. H. 2004, Hydrodynamic Stability, by P. G. Drazin and W. H. Reid, pp. 626. ISBN 0521525411. Cambridge, UK: Cambridge University Press, September 2004., 626
Dubrulle, B., Marié, L., Normand, C., et al. 2005, A&A, 429, 1
Dubrulle, B., & Zahn, J.-P. 1991, Journal of Fluid Mechanics, 231, 561
Dubrulle, B., & Knobloch, E. 1992, A&A, 256, 673
Fricke, K. 1968, ZAp, 68, 317
Goldreich, P., & Lynden-Bell, D. 1965, MNRAS, 130, 125
Goldreich, P., & Schubert, G. 1967, ApJ, 150, 571
Heifetz, E., Bishop, C. H., & Alpert, P. 1999, Quarterly Journal of the Royal Meteorological Society, 125, 2835
Hoskins, B. J., McIntyre, M. E., & Robertson, A. W. 1985, Quarterly Journal of the Royal Meteorological Society, 111, 877
Klahr, H. H., & Bodenheimer, P. 2003, ApJ, 582, 869
Klahr, H., & Hubbard, A. 2014, ApJ, 788, 21
Lerner, J., & Knobloch, E. 1988, Journal of Fluid Mechanics, 189, 117
Les, R., & Lin, M.-K. 2015, MNRAS, 450, 1503
Lesur, G., & Papaloizou, J. C. B. 2010, A&A, 513, A60
Li, H., Colgate, S. A., Wendroff, B., & Liska, R. 2001, ApJ, 551, 874

Li, H., Finn, J. M., Lovelace, R. V. E., & Colgate, S. A. 2000, ApJ, 533, 1023
Lin, M.-K., & Youdin, A. N. 2015, ApJ, 811, 17
Lobo Gomes, A., Klahr, H., Uribe, A. L., Pinilla, P., & Surville, C. 2015, ApJ, 810, 94
Lovelace, R. V. E., Li, H., Colgate, S. A., & Nelson, A. F. 1999, ApJ, 513, 805
Lyra, W. 2014, ApJ, 789, 77
Lyra, W., & Klahr, H. 2011, A&A, 527, A138
Marcus, P. S., Pei, S., Jiang, C.-H., & Hassanzadeh, P. 2013, Physical Review Letters, 111, 084501 (M13 in text)
Marcus, P. S., Pei, S., Jiang, C.-H., et al. 2015, ApJ, 808, 87
Meheut, H., Casse, F., Varniere, P., & Tagger, M. 2010, A&A, 516, A31
Meheut, H., Yu, C., & Lai, D. 2012, MNRAS, 422, 2399
Nelson, R. P., Gressel, O., & Umurhan, O. M. 2013, MNRAS, 435, 2610
Papaloizou, J. C. B., & Pringle, J. E. 1984, MNRAS, 208, 721
Petersen, M. R., Julien, K., & Stewart, G. R. 2007, ApJ, 658, 1236
Petersen, M. R., Stewart, G. R., & Julien, K. 2007, ApJ, 658, 1252
Lord Rayleigh 1880, Proc. Royal Math. Soc., 9, 57
Rincon, F., Ogilvie, G. I., & Cossu, C. 2007, A&A, 463, 817
Stoll, M. H. R., & Kley, W. 2014, A&A, 572, A77
Tamarin, T., Heifetz, E., Umurhan, O. M., & Yellin, R. 2015, Theoretical and Computational Fluid Dynamics, 29, 205
Turner, N. J., Fromang, S., Gammie, C., et al. 2014, Protostars and Planets VI, 411
Umurhan, O. M. 2010, A&A, 521, A25
Umurhan, O. M., Nelson, R. P., & Gressel, O. 2015, arXiv:1505.01892
Urpin, V. 2003, A&A, 404, 397
Urpin, V., & Brandenburg, A. 1998, MNRAS, 294, 399

APPENDIX

TWO DIMENSIONAL ANALYTICAL SOLUTIONS

For the extreme limiting case that $\epsilon = 0$ the asymmetric jet profile can be rendered into piecewise linear profiles. We have, four regions in which the perturbation vorticity field $\hat{\zeta} = 0$: "Zone I" for $x < -\Delta^-$, "Zone II" for $-\Delta^- < x < 0$, "Zone III" for $0 < x < \Delta^+$, "Zone IV" for $x > \Delta^+$. In each of these separate zones the normal mode stream function is given by

$$\hat{\psi}_{\mathrm{I}} = A e^{\alpha(x+\Delta^-)}, \qquad (A1)$$

$$\hat{\psi}_{\mathrm{II}} = A_+ e^{\alpha x} + A_- e^{-\alpha x}, \qquad (A2)$$

$$\hat{\psi}_{\mathrm{III}} = B_+ e^{\alpha x} + B_- e^{-\alpha x}, \qquad (A3)$$

$$\hat{\psi}_{\mathrm{IV}} = B e^{-\alpha(x-\Delta^+)}. \qquad (A4)$$

The velocity fields in each region may be immediately inferred from these above forms. Additionally, the normal mode pressure field $\hat{\Pi}$ may also be determined from the normal mode reexpression of equation (10) which is

$$\hat{\Pi} = \left(\frac{\omega}{\alpha} - v_0\right)\frac{d\hat{\psi}}{dx} + \left(2\Omega_0 + v_{0x}\right)\hat{\psi} \qquad (A5)$$

Solutions in each zone must be matched to one another subject to the continuity of the normal (perturbation) velocities and pressures at each transition zone $x = 0, \pm\Delta^\pm$ which amounts to six conditions

$$\hat{\psi}_{\mathrm{I}}(-\Delta^-) = \hat{\psi}_{\mathrm{II}}(-\Delta^-), \qquad \hat{\psi}_{\mathrm{II}}(0) = \hat{\psi}_{\mathrm{III}}(0),$$
$$\hat{\psi}_{\mathrm{III}}(\Delta^+) = \hat{\psi}_{\mathrm{IV}}(\Delta^+), \qquad (A6)$$

and

$$\hat{\Pi}_{\mathrm{I}}(-\Delta^-) = \hat{\Pi}_{\mathrm{II}}(-\Delta^-), \qquad \hat{\Pi}_{\mathrm{II}}(0) = \hat{\Pi}_{\mathrm{III}}(0),$$
$$\hat{\Pi}_{\mathrm{III}}(\Delta^+) = \hat{\Pi}_{\mathrm{IV}}(\Delta^+), \qquad (A7)$$

for the six unknowns $A, A_\pm, B, B_\pm$. Nontrivial solutions exist only if the determinant of the resulting matrix system is equal to zero which imposes a condition on the eigenvalue ω quoted in text equation (55). For the special restricted condition upon ω_a^- expressed in equation (54) we have

$$a\left(\omega_a^+, \alpha\Delta^+, \delta\right) = \frac{1}{2}\alpha\Delta^+(4\omega_a^+ + 3\delta - 3), \qquad (A8)$$

and

$$b\left(\omega_a^+, \alpha\Delta^+, \delta\right) =$$
$$\frac{1}{4}\left(\omega_a^+\right)^2 \left[-1 + e^{-2\alpha\Delta^+} - \frac{1}{\delta^2} + \frac{e^{-2\alpha\delta\Delta^+}}{\delta^2} - \frac{1}{\delta} + \right.$$
$$\frac{e^{-2\alpha\delta\Delta^+} - e^{-2\alpha(1+\delta)\Delta^+}}{\delta} + 2\alpha\Delta^+\frac{\delta+1}{\delta} + 4\left(\alpha\Delta^+\right)^2\right] +$$
$$\left(\alpha\Delta^+\right)^2\left(-\frac{9}{4}\delta - \frac{3}{2}\omega_a^+ + \frac{3}{2}\omega_a^+\delta\right), \qquad (A9)$$

and

$$c\left(\omega_a^+, \alpha\Delta^+, \delta\right) = e^{-2\alpha(1+\delta)\Delta^+}\frac{(1+\delta)\omega_a^+}{8\delta^2} \times$$
$$\left[\omega_a^+ + e^{2\alpha\Delta^+}\left(-\omega_a^+ + (\alpha\Delta^+)(-3 + 2\omega_a^+)\right)\right] \times$$
$$\left[\omega_a^+ + e^{2\alpha\delta\Delta^+}\left(-\omega_a^+ + \delta(\alpha\Delta^+)(3\delta + 2\omega_a^+)\right)\right] \qquad (A10)$$